AD-A166 715 INTERACTION OF SEISMIC WAVES WITH COMPLEX STRUCTURES 1/1
(U) CALIFORNIA INST OF TECH PASADENA SEISMOLOGICAL LAB
D V HELMBERGER ET AL. 21 MAY 85 SCIENTIFIC-2
UNCLASSIFIED AFGL-TR-85-0139 F19628-83-K-0010 F/G 8/11 NL

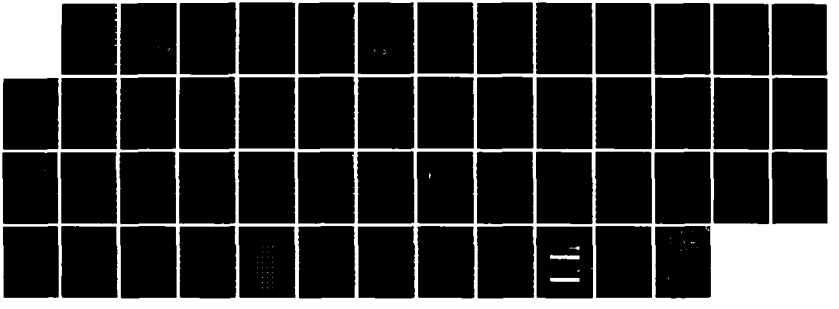

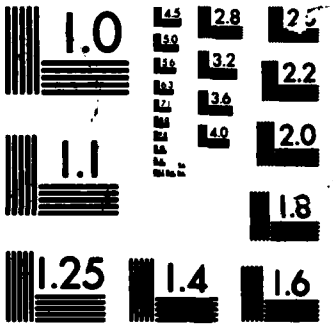

MICROCOPY CHART

(12)

AFGL-TR-85-0139

Interaction of Seismic Waves With Complex Structures

Donald V. Helmberger
David G. Harkrider
Robert W. Clayton

California Institute of Technology
Seismological Laboratory, 252-21
Pasadena, California 91125

21 May 1985

Scientific Report No. 2

APPROVED FOR PUBLIC RELEASE; DISTRIBUTION UNLIMITED

AIR FORCE GEOPHYSICS LABORATORY
AIR FORCE SYSTEMS COMMAND
UNITED STATES AIR FORCE
HANSCOM AIR FORCE BASE, MASSACHUSETTS 01731

This report has been reviewed by the ESD Public Affairs Office (PA) and is releasable to the National Technical Information Service (NTIS).

This technical report has been reviewed and is approved for publication.

John J. Cipar

JOHN J. CIPAR
Contract Manager

John J. Cipar acting for

HENRY A. OSSING, Chief
Solid Earth Geophysics Branch

FOR THE COMMANDER

Donald H. Eckhardt

DONALD H. ECKHARDT, Director
Earth Sciences Division

Qualified requestors may obtain additional copies from the Defense Technical Information Center. All others should apply to the National Technical Information Service.

If your address has changed, or if you wish to be removed from the mailing list, or if the addressee is no longer employed by your organization, please notify AFGL/DAA, Hanscom AFB, MA 01731. This will assist us in maintaining a current mailing list.

Do not return copies of this report unless contractual obligations or notices on a specific document requires that it be returned.

Unclassified

SECURITY CLASSIFICATION OF THIS PAGE

AD-A164715

REPORT DOCUMENTATION PAGE

1a. REPORT SECURITY CLASSIFICATION: Unclassified	1b. RESTRICTIVE MARKINGS
2a. SECURITY CLASSIFICATION AUTHORITY	3. DISTRIBUTION/AVAILABILITY OF REPORT: Approved for public release; distribution unlimited
2b. DECLASSIFICATION/DOWNGRADING SCHEDULE	
4. PERFORMING ORGANIZATION REPORT NUMBER(S)	5. MONITORING ORGANIZATION REPORT NUMBER(S): AFGL-TR-85-0139
6a. NAME OF PERFORMING ORGANIZATION: California Institute of Technology; 6b. OFFICE SYMBOL (If applicable)	7a. NAME OF MONITORING ORGANIZATION: Air Force Geophysics Laboratory
6c. ADDRESS (City, State and ZIP Code): Seismological Laboratory, 252-21 Pasadena, California 91125	7b. ADDRESS (City, State and ZIP Code): Hanscom AFB Massachusetts 01731
8a. NAME OF FUNDING/SPONSORING ORGANIZATION; 8b. OFFICE SYMBOL (If applicable)	9. PROCUREMENT INSTRUMENT IDENTIFICATION NUMBER: F19628-83-K-0010
8c. ADDRESS (City, State and ZIP Code)	10. SOURCE OF FUNDING NOS.

PROGRAM ELEMENT NO.	PROJECT NO.	TASK NO.	WORK UNIT NO.
62101F	7600	09	AE

11. TITLE (Include Security Classification): Interaction of Seismic Waves With Complex Structures

12. PERSONAL AUTHOR(S): Donald V. Helmberger, David G. Harkrider, Robert W. Clayton

13a. TYPE OF REPORT	13b. TIME COVERED	14. DATE OF REPORT (Yr., Mo., Day)	15. PAGE COUNT
Sci. Rpt. #2	FROM 1-12-84 TO 1-11-85	May 21, 1985	54

16. SUPPLEMENTARY NOTATION

17. COSATI CODES		
FIELD	GROUP	SUB. GR.

18. SUBJECT TERMS (Continue on reverse if necessary and identify by block number): Propagation in laterally varying media.

19. ABSTRACT (Continue on reverse if necessary and identify by block number)

Recent models of earth structure suggest large horizontal gradients, especially in shear velocities. Some changes in existing methods are required to construct synthetics for broad-band signals in many situations, especially when energy can reach the receiver by up-going as well as down-going paths. This can be accomplished by allowing locally dipping structure and making some modifications to generalized ray theory. Local ray parameters are expressed in terms of a global reference which allows a de Hoop contour to be constructed for each generalized ray with the usual application of the Cagniard-de Hoop technique. Synthetics generated from this method are compared with finite-difference runs using an advanced stable free-surface boundary condition where lateral velocity and density variations at the free surface are treated properly. The method is implicit, but only requires a simple pentadiagonal system solver to implement. When coupled with second- and fourth-order interior solutions, the overall problem appears to be stable for shear to compressional wave velocity greater than 0.01 and 0.02, respectively. The method is compared with other published algorithms for accuracy and stability. Keywords:

20. DISTRIBUTION/AVAILABILITY OF ABSTRACT	21. ABSTRACT SECURITY CLASSIFICATION
UNCLASSIFIED/UNLIMITED ☐ SAME AS RPT. ☒ DTIC USERS ☐	Unclassified

22a. NAME OF RESPONSIBLE INDIVIDUAL	22b. TELEPHONE NUMBER (Include Area Code)	22c. OFFICE SYMBOL
John J. Cipar	(617) 861-3746	AFGL/LWH

DD FORM 1473, 83 APR EDITION OF 1 JAN 73 IS OBSOLETE.

SECURITY CLASSIFICATION OF THIS PAGE

SCIENTIFIC REPORT NO. 2.

January 12, 1984 - January 11, 1985

Name of Contractor:	California Institute of Technology
Effective Date of Contract:	11 January 1983
Contract Expiration Date:	11 January 1986
Amount of Contract:	$273,547
Contract Number:	F19628-83-K-0010
Principal Investigators:	Donald V. Helmberger (818) 356-6998
	David G. Harkrider (818) 356-6910
	Robert W. Clayton (818) 356-6909
Program Manager and Telephone Number:	Dr. John Cipar (617) 861-3746
Short Title of Work:	Interaction of Seismic Waves With Complex Structures

The views and conclusions contained in this document are those of the authors and should not be interpreted as necessarily representing the official policies.

Sponsored by
Solid Earth Geophysics Branch
Earth Sciences Division
Department of the Air Force
Air Force Geophysics Laboratory (AFSC)
Hanscom Air Force Base, Massachusetts 01731

TABLE OF CONTENTS

I. SUMMARY

The research performed under this contract, during the period of 12 January 1984 through 11 January 1985, involved several tasks including:

(a) Development of computer programs for an elastic Kirchoff method to handle SH, SV, and P interactions.

(b) Simulation of complex structures for given velocity models and source properties and testing against numerical methods.

(c) Development of analytical theory to treat high-frequency propagation in laterally varying structure.

This report will discuss two aspects of our progress, namely the analytical developments in treating laterally varying structure and numerical extensions in theory to handle the air-ground interface problem.

In section II, we present some extensions of WKBJ and generalized ray theory for line and point sources, Helmberger et. al (1985). In particular, some changes in existing methods are required to construct synthetics for broad-band signals in many situations, especially when energy can reach the receiver by up-going as well as down-going paths. This can be accomplished by allowing locally dipping structure and making some modifications to generalized ray theory. Local ray parameters are expressed in terms of a global reference which allows a de Hoop contour to be constructed for each generalized ray with the usual application of the Cagniard-de Hoop technique. Several useful approximations of ray expansions and WKBJ theory are presented. Comparisons of the synthetics produced by these two basic techniques alone or in combination with known solutions demonstrates their reliability and limitations. In section III, we present a technique for improving the stability of finite- difference calculations at a free surface, Vidale

and Clayton (1985) where a stable free-surface boundary condition is derived for finite-difference solutions of the two-dimensional elastic wave equation. Lateral velocity and density variations at the free surface are correctly treated. The method is implicit, but only requires a simple pentadiagonal system solver to implement. When coupled with second- and fourth-order interior solutions, the overall problem appears to be stable for shear to compressional wave velocity greater than 0.01 and 0.02, respectively. The method is compared with other published algorithms for accuracy and stability.

II. Notes On Wave Propagation In Laterally Varying Structure

Considerable progress has been made recently in speeding-up the synthesizing of seismograms with the introduction of WKBJ and Gaussian beam methods, see Chapman (1978) and Cerveny et al. (1982). These methods have proven highly useful in generalizations to laterally varying structure, especially at high frequency, see for example Frazer and Phinney (1980). However, in the construction of longer periods (long period WWSSN seismograms) we many times are interested in more complete solutions, since the beginning portion of surface waves become important, see Grand and Helmberger (1984a). A complete set of ray parameter contributions is required to construct seismograms in this situation. In particular, one needs to consider ray paths leaving the source horizontally, a case where the WKBJ method breaks down. We can avoid this problem by applying a mixture of generalized ray theory, GRT, and WKBJ or Disk rays as defined by Wiggins (1976).

A simple example of this procedure is given in Fig. 1 where we show schematically how to construct the step response for a smooth velocity model approximated by a stack of homogeneous layers. We suppose that a velocity model can be chosen such that the step response remains a step at all receiver positions. The simulation of this step can be achieved by summing the response from three energy paths; namely, the direct, the reflected from just below the source or reference plane, and the diving WKBJ contribution. All three paths contain a product of the transmission coefficients above the source. The WKBJ path includes the transmission coefficients across the reference plane, taken as the interface below the source. We have included a diagram of the $\Theta(t)$ vs. p curve in Fig. 1 for reference as it clearly shows that the diving path contributes little except at the larger distances. At the nearest distance, position 1, the direct ray dominates. The reflected path contributes some as critical angle is approached. At still larger distances, position 3, a head wave along the bottom of the reference interface develops followed by the critically reflected pulse. The head wave contribution is included in the reflected

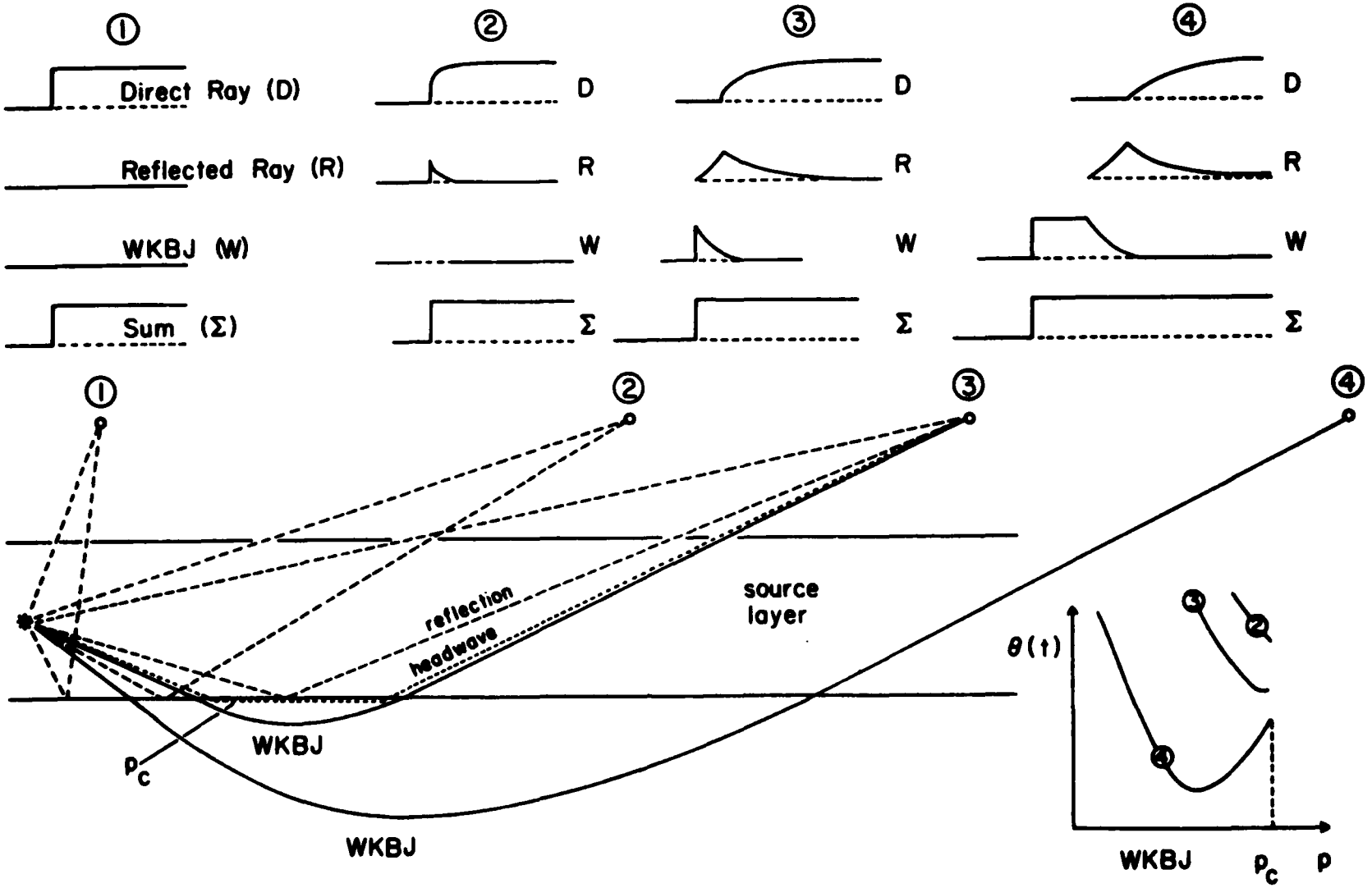

Figure 1: Schematic picture of ray paths and summation response for a smooth velocity gradient specified by a layered stack. Reflected and headwave paths for case 4 are omitted.

response since it is associated with the reflected generalized ray. At large ranges, the WKBJ contribution becomes increasingly dominant. Note that the WKBJ response turns off at the same time as the head wave starts because the transmission coefficient drops to zero. Essentially, combining the generalized rays and WKBJ response eliminates the truncation phase and avoids the turning point break-down of the WKBJ theory.

In testing the accuracy of the above procedure it is quite useful to generate the step response for models for which the answer is known. Thus, we begin with a homogeneous fluid whole space with a point source excitation yielding a step response at all positions with 1/(distance) decay. We next impose a spherical coordinate system with many thin shells of constant velocity. Applying the classical earth-flattening approximation we obtain a model with a smooth velocity increase in depth, see Helmberger (1973). The synthetics generated in Fig. 2 are from such a model with the exact step responses indicated by the dotted lines in the bottom panel. This panel also displays the response after summing the complete set of generalized rays; direct plus rays reflected upward from all the interfaces below the source. The GRT response at the largest distance shows the most roughness for times near the direct arrival when the interaction with the reflection from just below the source is the most severe. Similar complexity occurs with the hybrid method except that the diving energy is smoother with WKBJ. Short period synthetics generated from these step responses become quite dirty and simple geometric ray theory yields cleaner results. However, for most studies the advantage of being able to include the radiation pattern appropriate for earthquake sources, or shear dislocations, far outweighs the disadvantage of the noise generated by the hybrid method. For example, consider the SH-radiation from a dip-slip event where the up-going radiation has opposite polarity from the down-going energy, see Helmberger (1973). In short, the sum as displayed in Fig. 2 becomes more interesting when the direct ray trace has opposite sign from the other two.

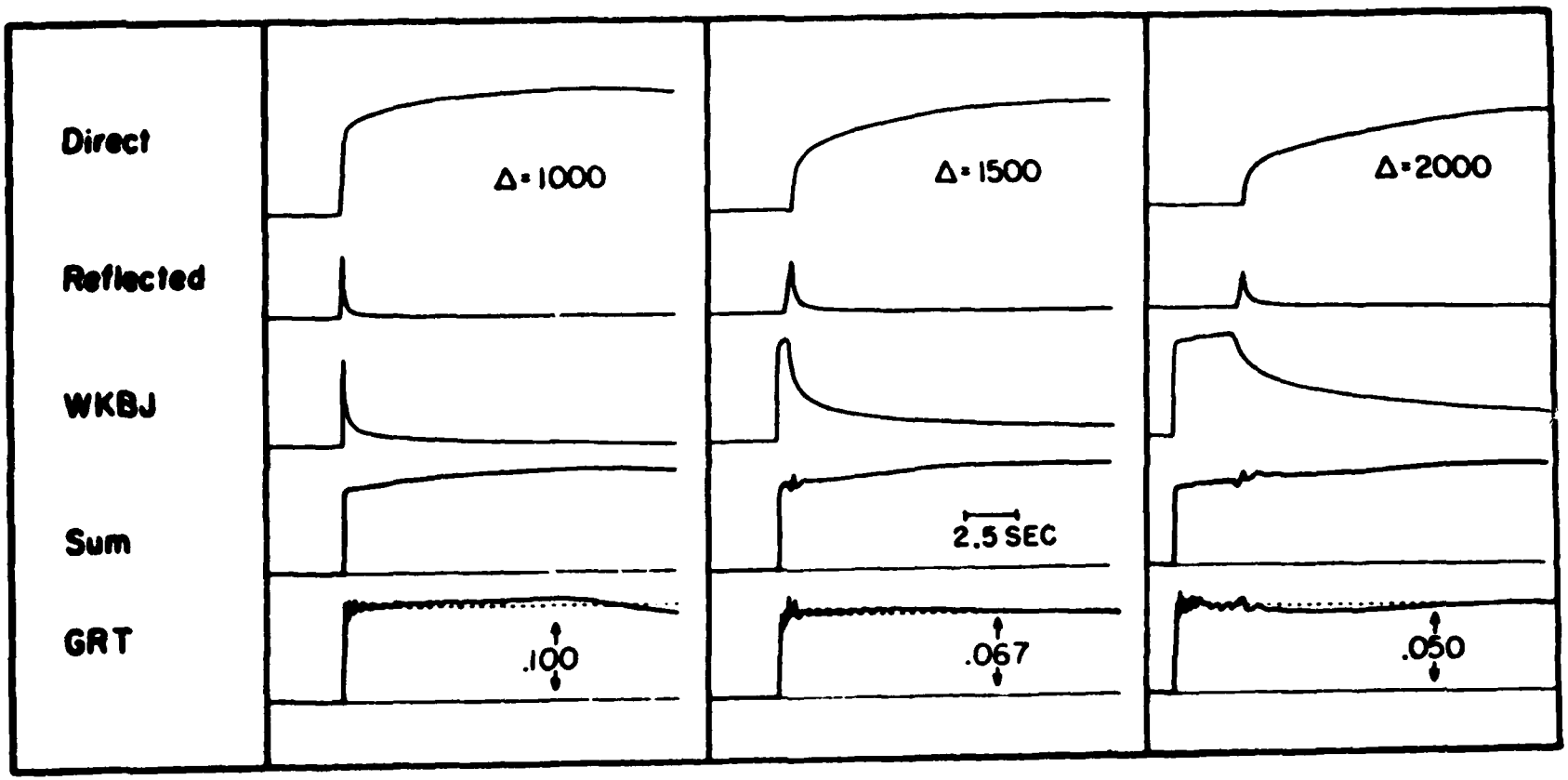

Figure 2: Synthetic step responses computed at three interesting distances and constructed by summing the three energy paths displayed in Fig. 1. The exact answer is indicated by the dotted response in the lower panel.

We could probably improve the response at the time the three energy paths interfere the most vigorously by including a few more GR's and/or by lowering the reference boundary for the WKBJ contribution. However, we are particularly interested in more realistic earth models with a sedimentary cover over bedrock or a crust-over-mantle structure providing natural reference boundaries. Thus, we propose using GR's to compute the start of the Love waves, and WKBJ to generate the responses returning from deeper structure. This approach proved effective in studying the structure and evolution of the lithosphere for an old oceanic plate, Grand and Helmberger (1984b). It would be advantageous to treat the obvious lateral variation encountered in such studies. Although the real world is truly three dimensional, some useful progress can be made by examining profiles of data along paths of symmetry where two-dimensional idealizations are appropriate. We will address such models in this paper.

Our strategy is similar to Wiggins (1976) in that we will use a combination of GRT and DRT to generate synthetics and justify the latter by demonstrated accuracy.

Review of Ray interactions with nonplanar structure

Boundary value problems involving complicated geometry have a long rather unrewarding history; thus, we will jump directly to approximate solutions and test their validity against finite-difference calculations and other more well-known results. Before addressing the dipping layer problem it is instructive to examine the flat-layered case and emphasize the geometric interpretation of generalized ray theory. This proves particularly useful for constructing generalizations to more complicated situations since the most progress in understanding these problems is at high frequency. Both line and point sources will be discussed since the former is easier to understand theoretically and for testing against numerical results, while the latter is necessary for studying the Earth.

Line source and Planar Model

The solution of the scalar wave equation assuming line source excitation for generalized rays as given by Gilbert and Knopoff (1961) is

$$\Phi_L(r,z,t) = H(t-t_o)/(t^2-t_o^2)^{1/2} \tag{1}$$

where $t_o = R/\alpha, R^2 = z^2 + r^2$, and α = velocity.

Φ_L is defined as the displacement potential with the index L used to remind ourselves of the line excitation. A high frequency approximation of (1) is

$$\Phi_L = H(t-t_o)/(t-t_o)^{1/2}\sqrt{R} \tag{2}$$

and the motion decays with distance as the $\sqrt{R}$. The solution to the interface problem setup displayed in Fig. 3a is

$$\Phi_L(r,z,t) = \mathrm{Im}(\frac{1}{\eta_1}\frac{dp}{dt}T(p)) \tag{3}$$

where

$$t = p(d_1 + d_2) + h_1\eta_1 + h_2\eta_2 \tag{4}$$

$$\eta_i = (\frac{1}{\alpha_i^2} - p^2)^{1/2}$$

T (p) = Transmission coefficient

The symbol (Im) indicates the imaginary part of the complex product of the functions of ray parameter, see Helmberger (1983) for example. The ray parameter appropriate for the direct arrival path, p_o , can be obtained by

$$\frac{dt}{dp}(p_o) = 0, \text{and } d_1 - \frac{h_1 p_o}{\eta_1} = d_2 - \frac{h_2 p_o}{\eta_2} \tag{5}$$

But with

$$p_o = \frac{\sin\Theta_1}{\alpha_1} = \frac{\sin\Theta_2}{\alpha_2} \tag{6}$$

and, therefore,

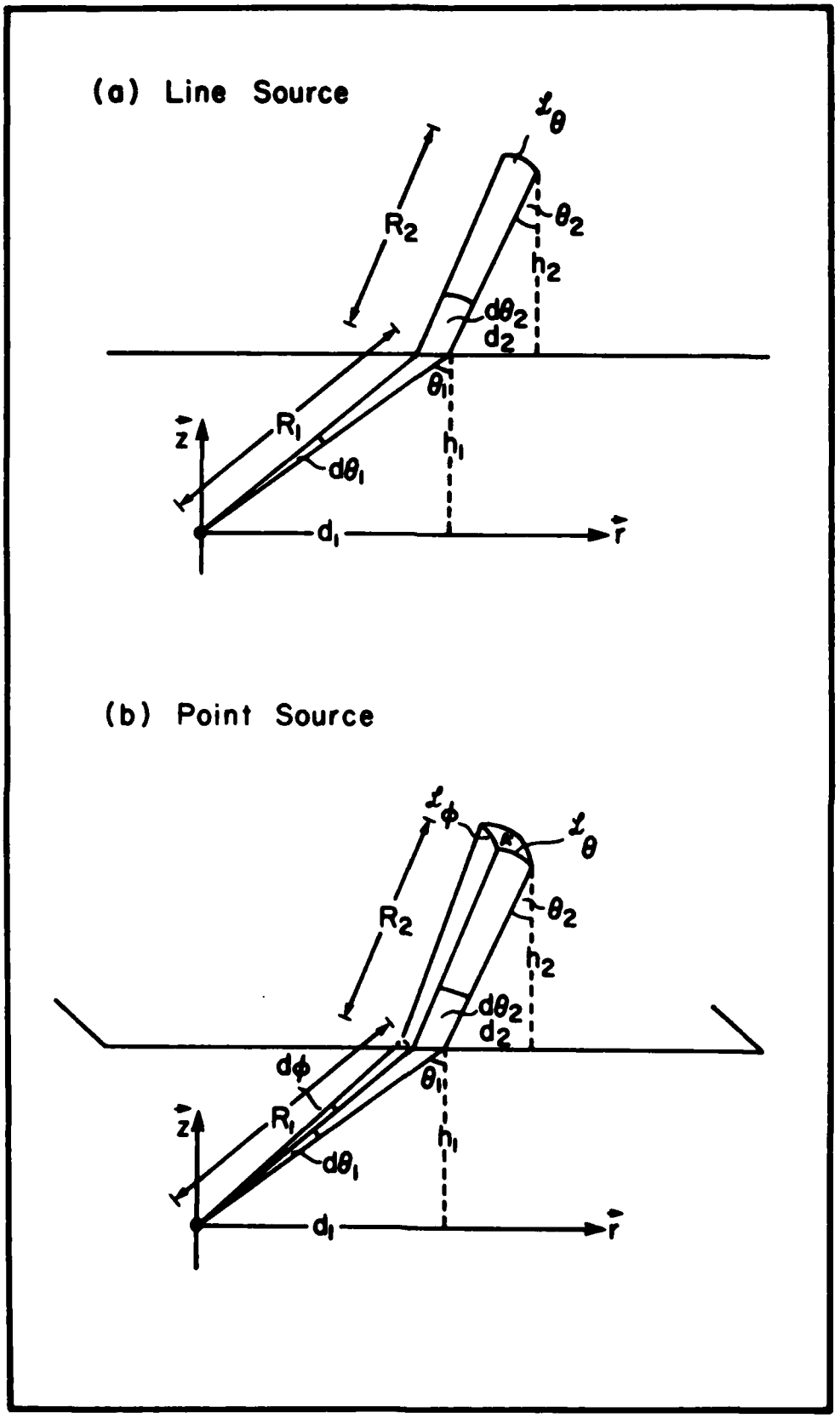

Figure 3: Diagram displaying the geometric spreading of ray tubes in two and three dimensions as they encounter a boundary.

$$\eta_1 = \frac{\cos\Theta_1}{\alpha_1}\ ,\ \eta_2 = \frac{\cos\Theta_2}{\alpha_2}$$

we see that the ray goes from the source to the receiver. And

$$t_o = \left\{\frac{\sin\Theta_1}{\alpha_1}d_1 + \frac{\cos\Theta_1}{\alpha_1}h_1\right\} + \left\{\frac{\sin\Theta_2}{\alpha_2}d_2 + \frac{\cos\Theta_2}{\alpha_2}h_2\right\} \tag{7}$$

$$t_o = R_1/\alpha_1 + R_2/\alpha_2$$

For times greater than t_o, we must solve t for complex p such that the imaginary parts of pd_1 and $\eta_1 h_1$ etc. cancel.

The behavior near p_o can be approximated by noting that

$$t = t_o + \frac{dt}{dp}(p - p_o) + \frac{d^2t}{dp^2}(p - p_o)^2/2$$

and solving for

$$(p - p_o)^2 = 2(t - t_o)/(\frac{d^2t}{dp^2})\ .$$

Thus,

$$\frac{dp}{dt} = (t - t_o)^{-1/2}/(2\frac{d^2t}{dp^2})^{1/2} \tag{8}$$

Note that from (4)

$$\frac{d^2t}{dp^2} = \frac{-h_1}{\eta_1^3\alpha_1^2} - \frac{h_2}{\eta_2^3\alpha_2^2} \tag{9}$$

It is convenient to condense the various factors containing p_o into

$$S_L(p_o) \equiv \frac{1}{|\frac{d^2t}{dp^2}|^{1/2}\sqrt{\alpha_1}\eta_1}, \tag{10}$$

which we call the spreading factor. Thus,

$$S_L = \left[\frac{h_1}{\eta_1\alpha_1} + \frac{h_2}{\eta_2\alpha_2}\left(\frac{\eta_1^2\alpha_1}{\eta_2^2\alpha_2}\right)\right]^{-1/2} \tag{11}$$

We note that by differentiating Snell's law we obtain

$$\frac{\cos\Theta_1}{\alpha_1} d\Theta_1 = \frac{\cos\Theta_2}{\alpha_2} d\Theta_2 .$$

Substituting this expression into S_L we obtain

$$S_L = \frac{\sqrt{d\Theta_1}}{\left[R_1 d\Theta_1 + R_2 d\Theta_2 \frac{\cos\Theta_1}{\cos\Theta_2} \right]^{1/2}} \tag{12}$$

If $R_2 = 0$, we obtain the whole space spreading again where $(R_1 d\Theta_1)$ is just the width of the ray tube described in Fig. 3a. A correction for the change in direction is required as the tube crosses the interface, namely

$$(\cos\Theta_1/\cos\Theta_2) .$$

Thus, the denominator of (12) is again the width of the ray tube at the receiver, L_Θ in Fig. 3a. Substituting into (3) we obtain

$$\Phi_L \; \alpha \; S_L H(t-t_o) Re\,(T(p_o))/(t-t_o)^{1/2} \tag{13}$$

where R_e indicates the real part operator.

Point source and Planar Model

The point source solution for the same problem setup, Fig. 3b, is

$$\Phi_p(r,z,t) = \sqrt{\frac{2}{r}} \frac{1}{\pi} \left[\frac{1}{\sqrt{t}} * Im\left(T(p) \frac{\sqrt{p}}{\eta_1} \frac{dp}{dt} \right) \right] \tag{14}$$

and applying the same first motion approximation we obtain a slightly more complicated spreading factor namely,

$$S_P \equiv \sqrt{\frac{p}{r}} \frac{1}{\eta_1} \left| \frac{d^2 t}{dp^2} \right|^{-1/2} \tag{15}$$

$$= \left[\frac{R_1 \sin\Theta_1 + R_2 \sin\Theta_2}{\sin\Theta_1} \right]^{-1/2} S_L \tag{16}$$

and note that by letting $R_2 = 0$ we obtain

$$S_P = 1/R \tag{17}$$

In terms of area, we note that

$$S_P = \left[\frac{\sin\Theta_1 d\Theta_1 d\Phi}{(R_1 \sin\Theta_1 d\Phi + R_2 \sin\Theta_2 d\Phi)(R_1 d\Theta_1 + R_2 d\Theta_2 \frac{\cos\Theta_1}{\cos\Theta_2})} \right]^{1/2} \tag{18}$$

which can be interpreted as the incremental element of area at the source divided by the projected area at the receiver or simply,

$$S_P = \left[\frac{A_o}{A} \right]^{1/2} . \tag{19}$$

Thus, the first motion behavior becomes

$$\Phi_p(r_1 t_1 t) = \frac{1}{\pi} \left[\frac{1}{\sqrt{t}} * \frac{1}{\sqrt{t - t_o}} \right] S_P \mathrm{Re}(T(p_o)) \tag{20}$$

$$= S_p H(t - t_o) \mathrm{Re}(T(p_o))$$

More complicated solutions to multi-layered models in terms of ray summations will be discussed later.

Locally Dipping Structure

Although GRT for parallel interfaces has been well developed the modifications for nonplanar structure or smoothly varying interfaces has not. Some of the difficulties encountered for the simple wedge problem have been discussed by Hudson (1963). Hong and Helmberger (1977) constructed a solution in terms of generalized rays for this problem and defined a method of ray path construction compatible with the usual Cagniard-de Hoop formalism. We will consider the direct arrival interacting with two dipping interfaces as an example application. The problem setup is displayed in Figure 4a with the response given by

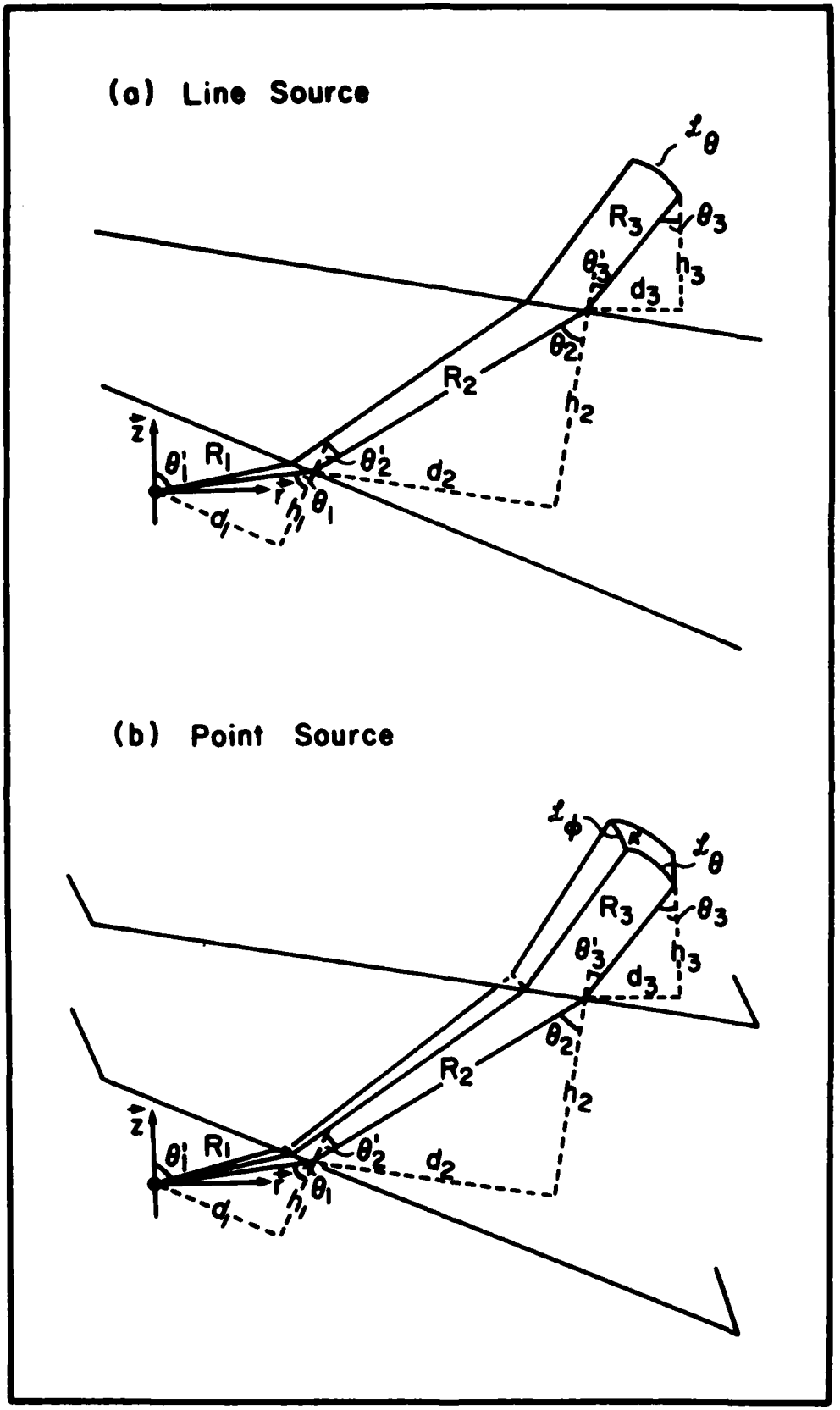

Figure 4: Diagram displaying the geometric spreading of rays encountering non-planar interfaces.

$$\Phi_L = \mathrm{Im}\left[T_{12} \frac{(p_1)\ T_{23}(p_2)1}{\eta_1} \frac{dp}{dt} \right] \tag{21}$$

where p_1 and p_2 are defined by the local ray parameter, namely

$$p_1 = \frac{\sin\Theta_1}{\alpha_1}\ ,\ p_2 = \frac{\sin\Theta_2}{\alpha_2}$$

and are no longer equal. However,

$$\frac{\sin\Theta_1}{\alpha_1} = \frac{\sin\Theta_2'}{\alpha_2}$$

where

$$\Theta_2' = \Theta_2 + \Theta_s$$

with Θ_s defining the change of the slope of interface (1) relative to the previous reference at Θ_1. Performing the derivatives discussed in the previous section we obtain

$$S_L(p_o) = \frac{\sqrt{d\Theta_1}}{\left[R_1 d\Theta_1 + R_2 d\Theta_2 \frac{\cos\Theta_1}{\cos\Theta_2'} + R_3 d\Theta_3 \frac{\cos\Theta_2}{\cos\Theta_2'} \frac{\cos\Theta_1}{\cos\Theta_2'} \right]^{1/2}}$$

which is similar to (12) and has the same interpretation. The travel time is defined by

$$t = \sum_{i=1}^{3} (p_i d_i + \eta_i h_i) \tag{22}$$

with the definitions of d_i and h_i given in Fig. 4a as the projection of the geometric path onto the local Cartesian coordinates. The arrival time can be determined as before with

$$\frac{dt}{dp_m} = o$$

defining

$$p_1 = p_{o_1}, p_2 = p_{o_2},$$

etc. Thus,

$$d_m - h_m \frac{p_m}{\eta_m} = 0 \tag{23}$$

with

$$p_m = \frac{\sin\Theta_m}{\alpha_m} \quad \text{and} \quad \eta_m = \frac{\cos\Theta_m}{\alpha_m}$$

and the $\frac{dt}{dp_m} = 0$ condition leads to a ray going from the source to the receiver. The first-motion approximation becomes

$$\Phi_L \;\alpha\; \mathrm{Re}(T_{12}(p_{o_1})T_{23}(p_{o_2}))\frac{H(t-t_0)}{(t-t_o)^{1/2}}S_L \tag{24}$$

Spreading for the point source solution becomes slightly more complicated than in the flat case, but allowing

$$\sqrt{\frac{r}{p}} = \left[\sum_{i=1}^{3}\frac{d_i}{p_i}\right]^{1/2} \tag{25}$$

results in S_P defined by

$$S_P = \sqrt{\frac{p}{r}}\frac{1}{\eta_1}\left|\frac{d^2t}{dp^2}\right|^{-1/2} \tag{26}$$

reducing to

$$= (A_o/A)^{1/2},$$

at the direct arrival time. The details of this result have been given previously by Hong and Helmberger (1978). Thus, the point source solution for the geometry given in Fig. 4b becomes

$$\Phi_p = \frac{1}{\pi}\left[\frac{1}{\sqrt{t}} * \mathrm{Im}\left[\Pi(p)\frac{1}{\eta_1}\frac{dp}{dt}\left(\sum\left(\frac{d_i}{p_i}\right)\right)^{-1/2}\right]\right] \tag{27}$$

where

$$\Pi(p) = T_{12}(p_1)T_{23}(p_2)\ .$$

Numerical evaluation of (27) yields the geometric result but, also, retains longer period information since (dp/dt) can be evaluated along the de Hoop contour in the usual

manner. The accuracy of constructing broad-band synthetics applying this procedure is well known, see for example Apsel and Luco (1983) or Burdick and Orcutt (1978).

Many layers, WKBJ, and Radiation patterns

Following the results of the previous section, and inserting the radiation pattern for the simple SH motions from a dislocation source, see Helmberger and Malone (1975) the displacements can be written

$$v(r,z,\Theta,t) = \frac{M_o}{4\pi\rho_o}\left(\frac{\Delta}{\sin\Delta}\right)^{1/2}\frac{d}{dt}\left[\dot{D}(t) * \sum_{j=1}^{2} A_j(\Theta,\lambda,\delta) V_j(t)\right] \tag{28}$$

where

$$V_j(t) = \sqrt{\frac{2}{r}}\frac{1}{\pi}\left[\frac{1}{\sqrt{t}} * \Psi_j(t)\right] \tag{29}$$

and

$$\Psi_j(t) = \sum_{i=1}^{n} SH_j(p)\frac{\sqrt{p}}{\eta_\beta}(2p)C_o\frac{dp}{dt}\Pi_i(p) \tag{30}$$

and the summation of n rays is required. The various symbols are defined below:

$v(r,z,\Theta,t)$ = displacement on free surface

M_o = moment

ρ_o = density

D(t) = dislocation history

$\dot{D}(t)$ = far-field time function

$A_1(\Theta,\lambda,\delta) = \cos 2\Theta\cos\lambda\sin\delta - 1/2\sin 2\Theta\sin\lambda\sin 2\delta$,

$A_2(\Theta,\lambda,\delta) = -\sin\Theta\cos\lambda\cos\delta - \cos\Theta\sin\lambda\cos 2\delta$,

Θ = strike from the end of the fault plane

λ = rake angle

δ = dip angle

r = distance between source and receiver

p = ray parameter

$$\eta = \left(\frac{1}{\beta^2} - p^2\right)^{1/2}$$

Δ = epicentral distance in radians

$\left(\frac{\Delta}{\sin\Delta}\right)^{1/2}$ = correction for earth flattening

β = shear velocity

and where the vertical radiation patterns are given by

$$SH_1 = \frac{1}{\beta^2} \ ,$$

$$SH_2 = \frac{\epsilon}{\beta^2} \ \frac{\eta}{p} \ , \ \epsilon = \begin{matrix} +1 & z > h \\ -1 & z < h \end{matrix}$$

$$\eta = \left(\frac{1}{\beta^2} - p^2\right)^{1/2}$$

The correction for point source spreading is defined by

$$C_s = \sqrt{\frac{r}{p}}\left(\sum\frac{d_i}{p_i}\right)^{-1/2} \tag{31}$$

This solution is similar to the flat case and we can, obviously, construct the diving ray response for a smoothly varying structure by summing the primary rays as discussed in Fig. 2. We can then use this result to check the disk ray solution which can be obtained by replacing (30) by

$$\Psi_j = SH_j(p)\frac{\sqrt{p}}{\eta_\beta}(p)\sum(\delta p/\delta t) \tag{32}$$

where the sum is taken over the p (t) curve as described by Wiggins (1976).

For a simple turning ray problem

$$\left|\frac{\delta p}{\delta t}\right| = \frac{1}{|r - r(p)|} \tag{33}$$

where r(p) is distance reached by a ray defined by p, see Fig. 5. Substituting (33) into

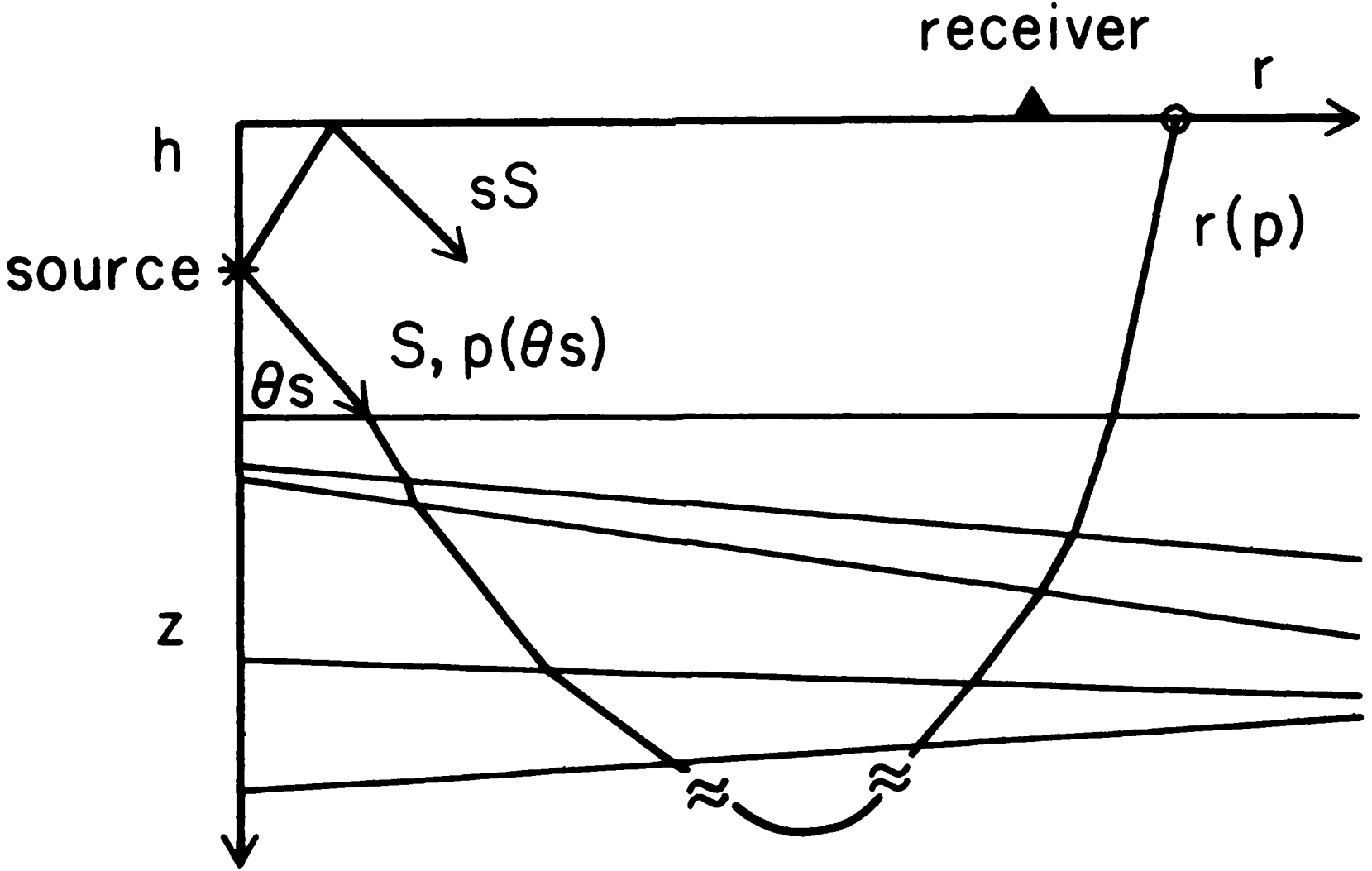

Figure 5: Ray geometry where the source and receiver are separated by r and the source depth is h. The ray starts with the $p = \sin\Theta_s/\beta$ and reaches the surface at r (p).

(32) and evaluating (29) yields a simple step response, as discussed by Chapman (1976). Essentially, (33) has a simple square-root singularity at r = r(p), and rays that hit the surface near the receiver dominate the behavior. Since p varies along the path, we must define which p to use in the evaluation of (32). The proper choice is the starting p at the source as outlined in the previous section. Note that for the case of an up-going direct ray the two methods can be interpreted in a similar manner. Only one ray is involved in both, and applying the first-motion approximation of (30) yields (32) where the extra (2) is produced by the double valued nature of expression (33). Thus, the application of WKBJ theory to the locally dipping problem appears to be essentially the same as for the uniform layered problem. We trace the ray through a stack of layers down to the turning region, turn it around analytically, and follow it to the surface obeying Snell's law. The special treatment at the turning point removes the nonlinear ray parameter effects of the homogeneous layered parameterization as is well known. Essentially, when the ray reaches critical angle at a given interface, we back up to the previous reference interface and compute the local linear velocity gradient. The travel time and location at which the ray recrosses the reference interface is easily calculated by analytical means. Such a procedure is compatible with the Langer approximation which is the basis for the WKBJ method, see Aki and Richards (1980). Earth stretching becomes slightly more complicated than in the uniform layered case. In this situation we let

$$ra_j = (r_j + r_{j+1})/2$$

where r_j is the radius of the Earth at the j th layer, etc., and ra_j becomes the radius at the layer's midpoint. The cross-section is then constructed in terms of vertical profiles of velocity and thickness vs. ra_j and the points connected by linear lines as displayed in Fig. 5. Next, the layer thickness, Th_j, are increased by

$$\tau_j = Th_j(r_o/ra_j)$$

where r_e is the radius of the Earth. Note that at this stage the horizontal velocity in each layer remains constant. The velocity-depth cross-sections will be presented in this format. The velocity and density approximations are determined as the ray encounters the various interfaces with

$$\beta = V_j(r_o/ra_j)$$

$$\rho_j = d_j(r_o/ra_j)$$

and ra_j is determined by the local layer thickness and position. Thus, the velocity is no longer constant in any given layer but depends on local depth correction. The C_e factor can be assumed to be one for most applications of gentle dipping structure, as discussed in the next section and was omitted from (32).

The approach followed here is similar to that followed by Wiggins (1976) in that the main justification for expression (33) is that it yields results comparable to GRT. A theoretical justification of applying WKBJ to laterally varying structure is given by Chapman and Drummond (1982). See Wesson (1970).

3. Applications

In this section we will briefly outline possible applications of these approximate solutions to seismological problems. First, the direct or up-going energy problem is discussed when motions in the sloping layers of a sedimentary basin are excited by a line-source. In this form Finite Difference calculations can be used to check the accuracy of the GRT results. Next, the point source excitation of Love waves is considered in the presence of sloping structure followed by models of growing Lithosphere. Finally, we construct synthetics for laterally varying upper mantle models and confirm the usefulness of WKBJ at long periods.

Local seismograms

One of many complexities associated with strong motion seismology is the noticeably long duration of high frequency P-waves observed in sedimentary basins. These waves are generally polarized onto the vertical component due to the strong velocity gradients near the surface. The latter portion of these observed motions are generally depleted at lower frequency. Thus, one might conclude that there are propagational waveguides that preferentially prolong high frequency motions. Non-planar surface layering appears to have this property. This calculation will be done with SH-waves since this type of motion is studied throughout the remainder of this paper, but we would expect that P-waves would behave in a similar manner.

A single low velocity layer which grows with distance between the source and receiver is assumed with a line source of SH motion situated at a depth of 5.5 km. The response build-up as a function of the number of multiples is displayed in Fig. 6. The square-root singularity indicated in expression (13) is apparent for the direct arrival. Note that after one bounce the reflection from the lower interface becomes complex because of the local ray parameter effect and a head wave and post-critical angle reflection develops. After two bounces, the time separation between the head wave onset and reflection times becomes less and the reflected spike increases in strength. After many bounces the ray can no longer reach critical angle and still fit into the waveguide. Thus, $(R)^n$ becomes small since the reflection coefficient (R) becomes less than one. The drop-off in amplitude of the multiples occurs abruptly at this time on the record.

The corresponding point source response displayed in Fig. 7 can be obtained from expression (29). Neglecting the C_s factor produces a similar response with a slight reduction in later arrivals, roughly 13% for the last arrival. Thus, point source amplitudes can be approximated quite well by scaling line source results by the square-root of the distance factor similar to the flat case. Note that the Cagniard-de Hoop technique proves particularly useful in tracing these rays and evaluating their individual

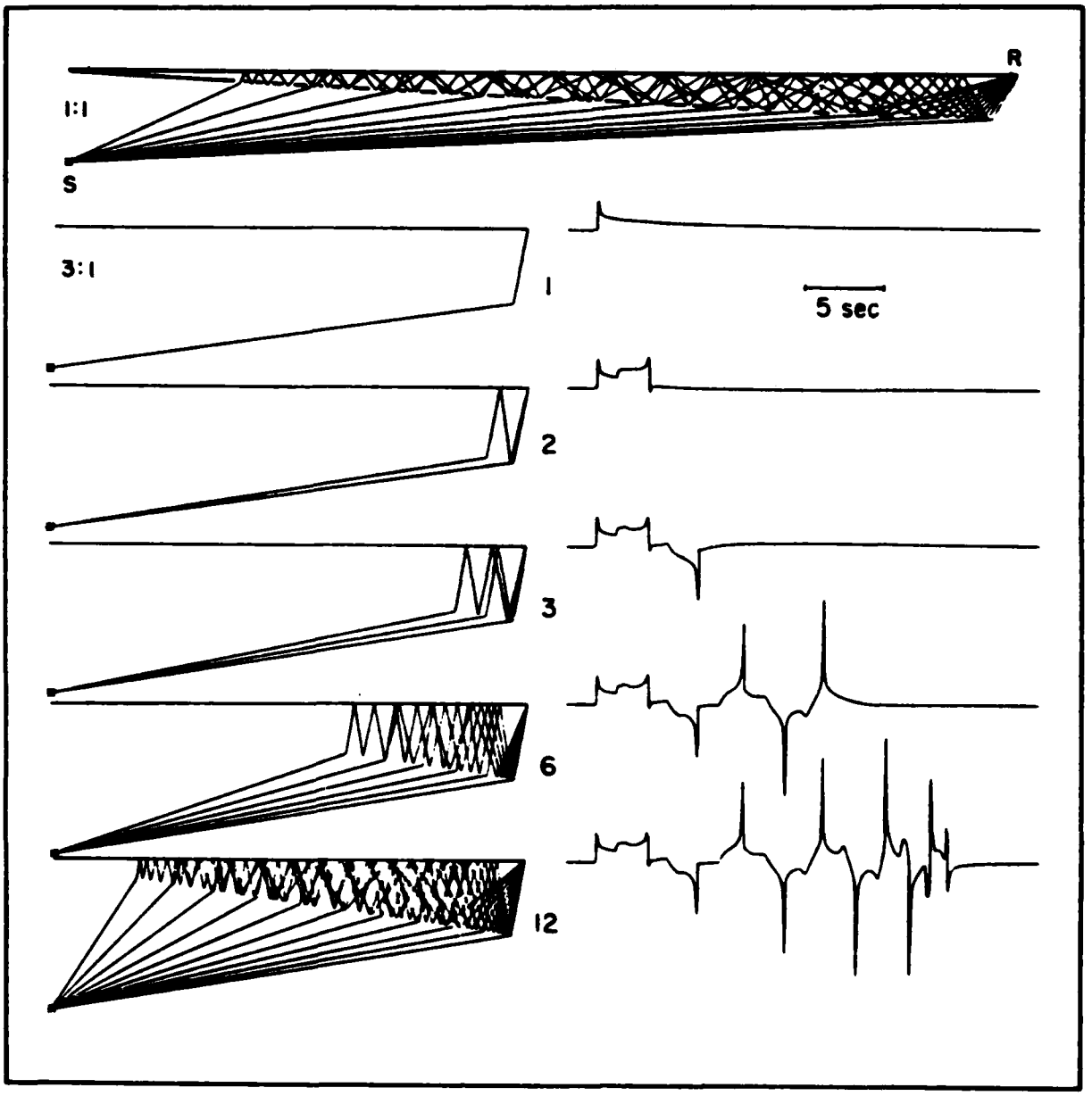

Figure 6: Line source response as a function of ray summation. The seismic parameters are $\beta_1 = 1.5$ km/sec, $\rho_1 = 1.5\ gm/cm^3$, and $\beta_2 = 3.3$, $\rho_2 = 2.5$ for the upper and lower layer respectively. The top plot displays the ray paths at ray parameters appropriate for Snell's law at true scale. Ray plots on the left have a vertical exaggeration of 3 to 1.

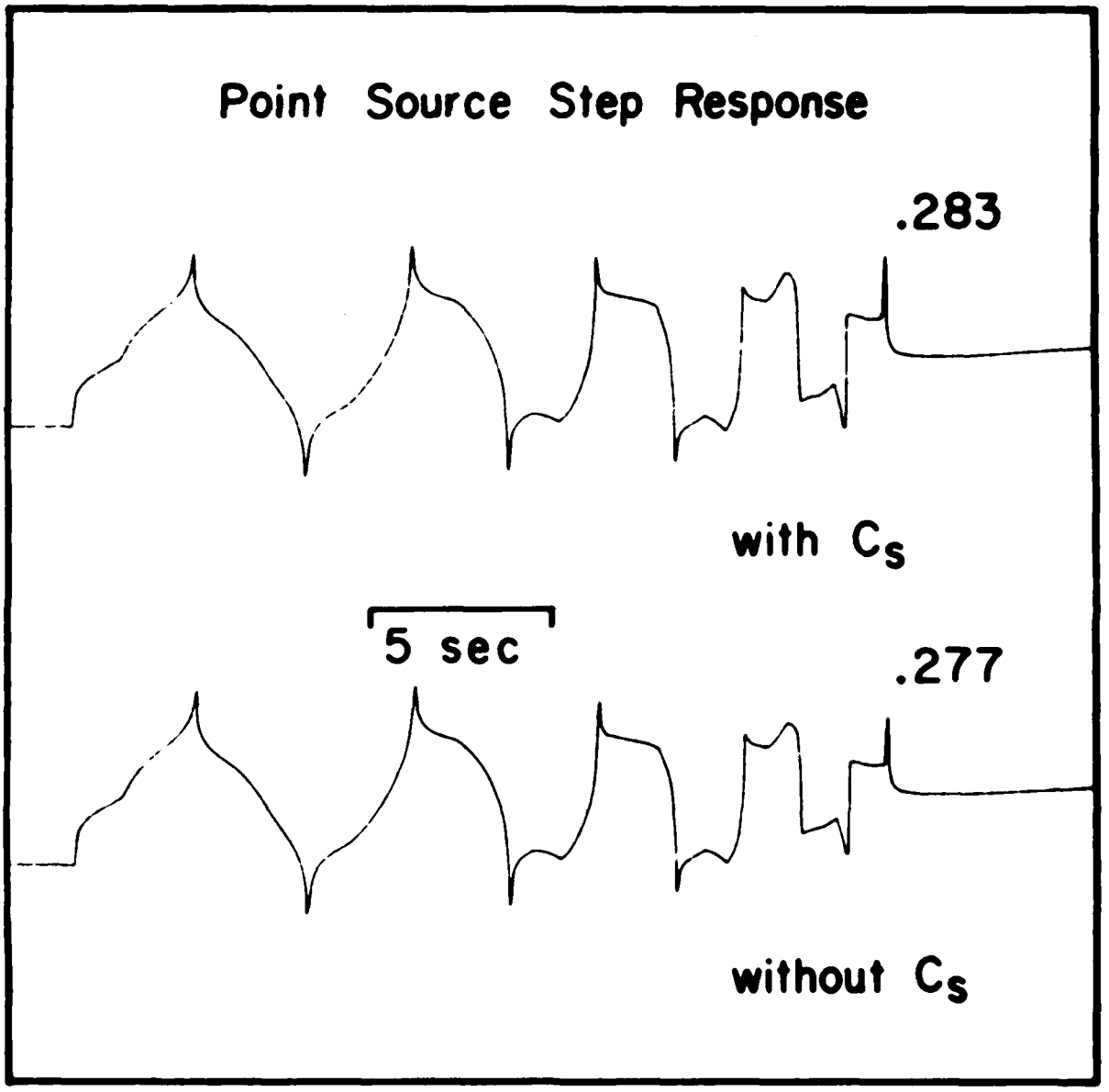

Figure 7: Step responses appropriate for a strike-slip double couple source and the model discussed in Fig. 6 with and without the C_s correction.

contributions. However, as mentioned earlier, this series of rays does not necessarily converge to the exact solution and some demonstration of accuracy is required. This was attempted earlier by Hong and Helmberger (1977) but not very convincingly. A much more rigorous comparison with a numerical code is presently being conducted by Vidale et al (1984) with preliminary results of the comparison of the two techniques for this simple model displayed in Fig. 8. The top trace is the broadband result displayed in Fig. 6., with a filtered response in the middle for comparison with finite-difference results on the bottom. The highest frequencies have been removed in this comparison due to computational expense but the existence of strong high frequency multiples is striking. Since the finite-difference calculation can be performed on any arbitrary two-dimensional structure we have extended the thin layer directly above the source to the left as a flat thin layer avoiding the wedge effect which is obviously omitted in the ray solution. Comparison with and without the wedge and many other complexities involving double-couple solutions constructed by line-to-point source operators are discussed in Vidale et al (1984). We will suppose throughout the remainder of this paper that the generalized ray modifications discussed in the previous section are sufficiently accurate to test the WKBJ synthetics.

Love waves at Regional Distances

Another interesting application of the above technique is in the development of Love waves and the effects of traveling across oceanic-to-continental transitions. This problem was encountered in a recent paper by Grand and Helmberger (1984b) when the so-called G-phase, the name applied to the impulsive Love waves associated with oceanic paths, interferes with mantle arrivals. Apparently, this situation occurs for well developed lithosphere associated with older plates over-lying slower upper-mantle velocity models. The beginning portions of the G-phase as recorded slightly inland develop longer periods than observed at island stations. Their period and arrival times are

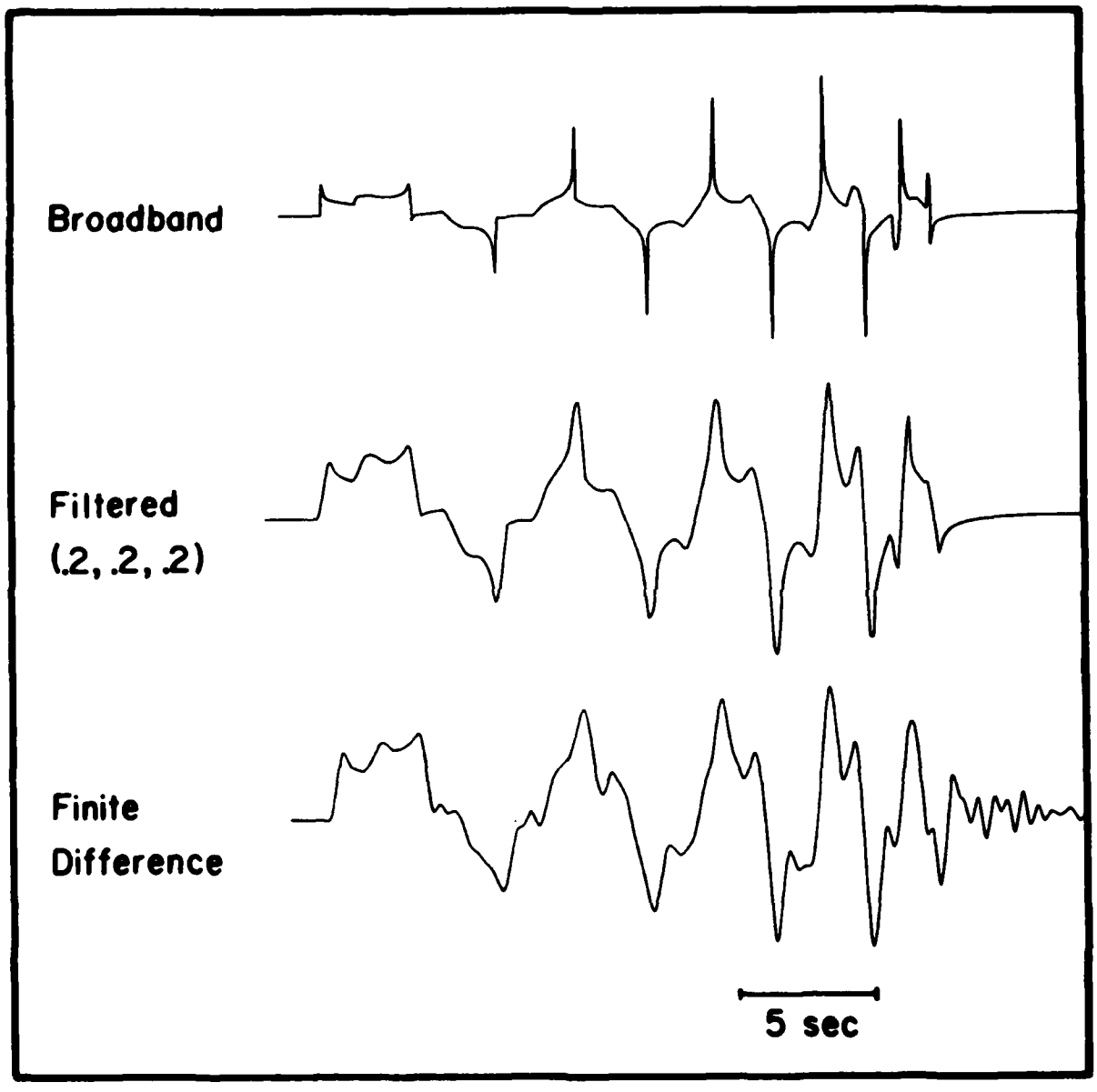

Figure 8: Comparison of GRT results with a finite-difference calculation. The broadband trace has been filtered to remove the high frequency spikes.

compatible with the model presented in Fig. 9a. A dipping model with arrival times compatible with the flat model is presented in Fig. 9b along with the comparison of step responses given on the right. Note that the first 45 sec of motion are nearly identical. The higher frequency portions of the Love wave become less pronounced in the dipping case but the general appearance is similar to the pure-oceanic case, see Grand and Helmberger (1984b).

It appears that as the lithosphere ages it gets thicker, for example, see Forsyth (1975). A preliminary model of predicted Love waves for this situation is given in Fig. 10, also included are synthetics for a fast and slow mantle. The long period nature of the synthetics from the dipping model is similar to the slow model as we might expect. However, there is considerable roughness at the start of the Love waves caused by the mixed paths involving both the crust and lid.

Observationally, we see upper-mantle arrivals starting near these ranges. Thus, the diving energy must be added to these synthetics following the strategy discussed earlier. This can be accomplished by summing GR's or by applying WKBJ.

Upper-mantle models

In this section we investigate effects of lateral variation in upper mantle models, as displayed in Fig. 11. We have chosen a particularly simple case with no low velocity zone to simplify the comparison of GRT with WKBJ synthetics. A further simplification is made by allowing the two models to be connected in a linear fashion as displayed in the middle column.

Following the WKBJ approach we first illuminate the model by tracking a set of rays from the source towards prospective receivers. These rays reach the surface at r(p) in time T(p). The travel time at a particular receiver, r, can be written $t(p) = p\,r + T(p) - p\,r(p)$. Note that p changes in each layer but they are all functions of the beginning p. Thus, we can construct the t versus p curves as displayed in Fig. 12 for reversed

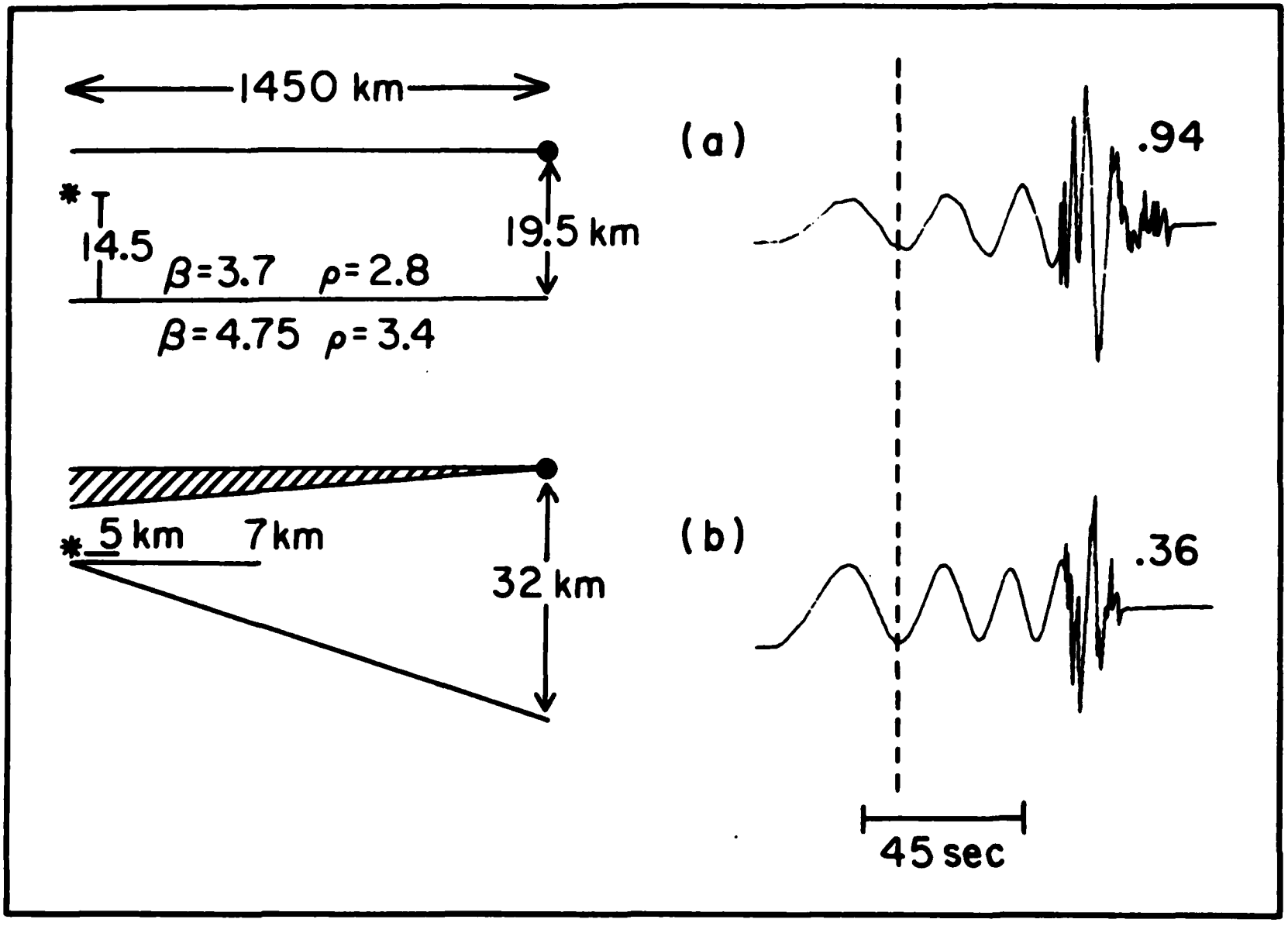

Figure 9: Flat and dipping models and corresponding step responses with peak amplitudes indicated on each trace. Note that the first 45 secs of each record are nearly identical in amplitude and shape when corrected by the scaling factors.

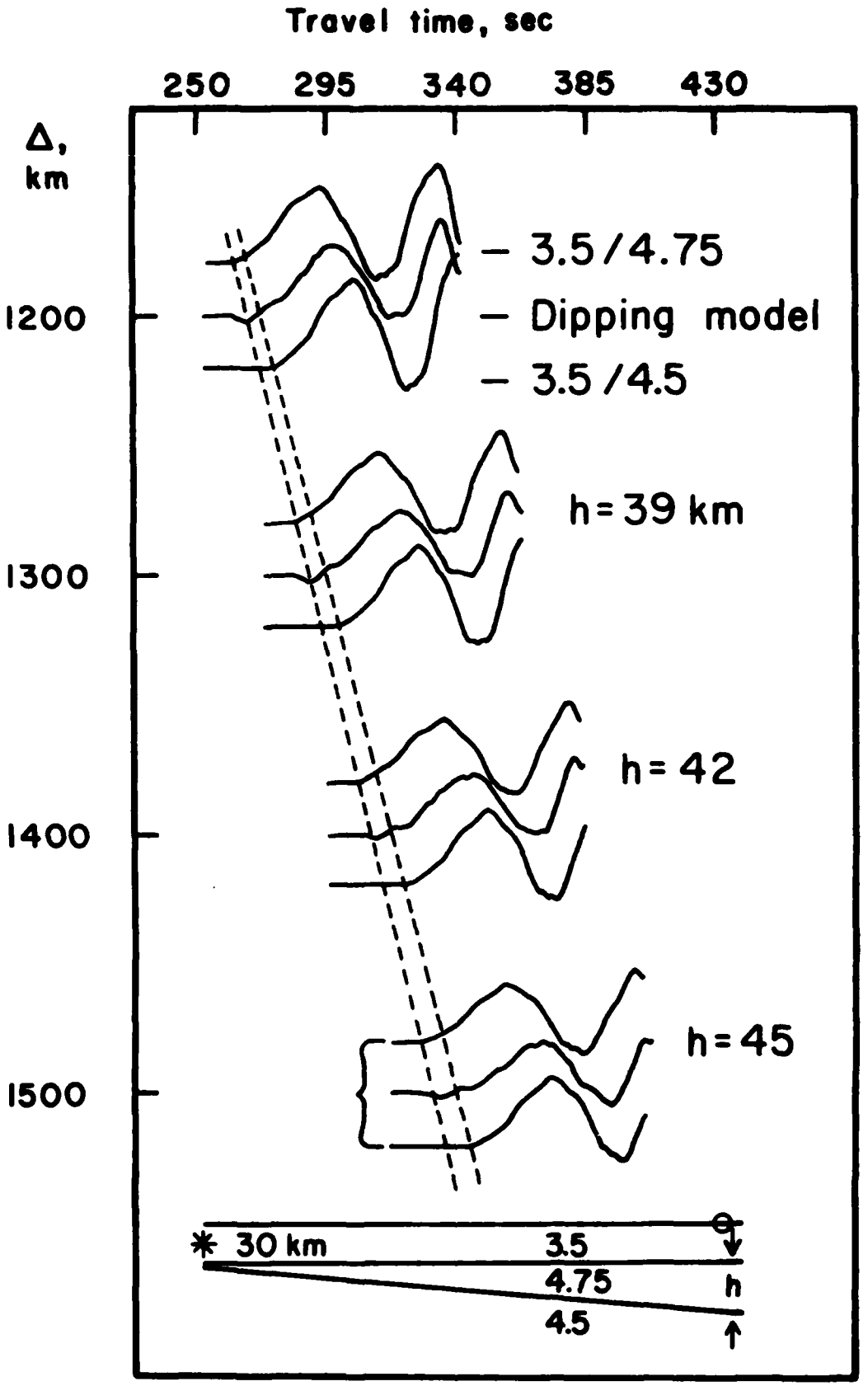

Figure 10: Comparison of step responses for two simple models with a model containing a growing high velocity lid. The dotted lines indicate the first arrival times of the two simple models.

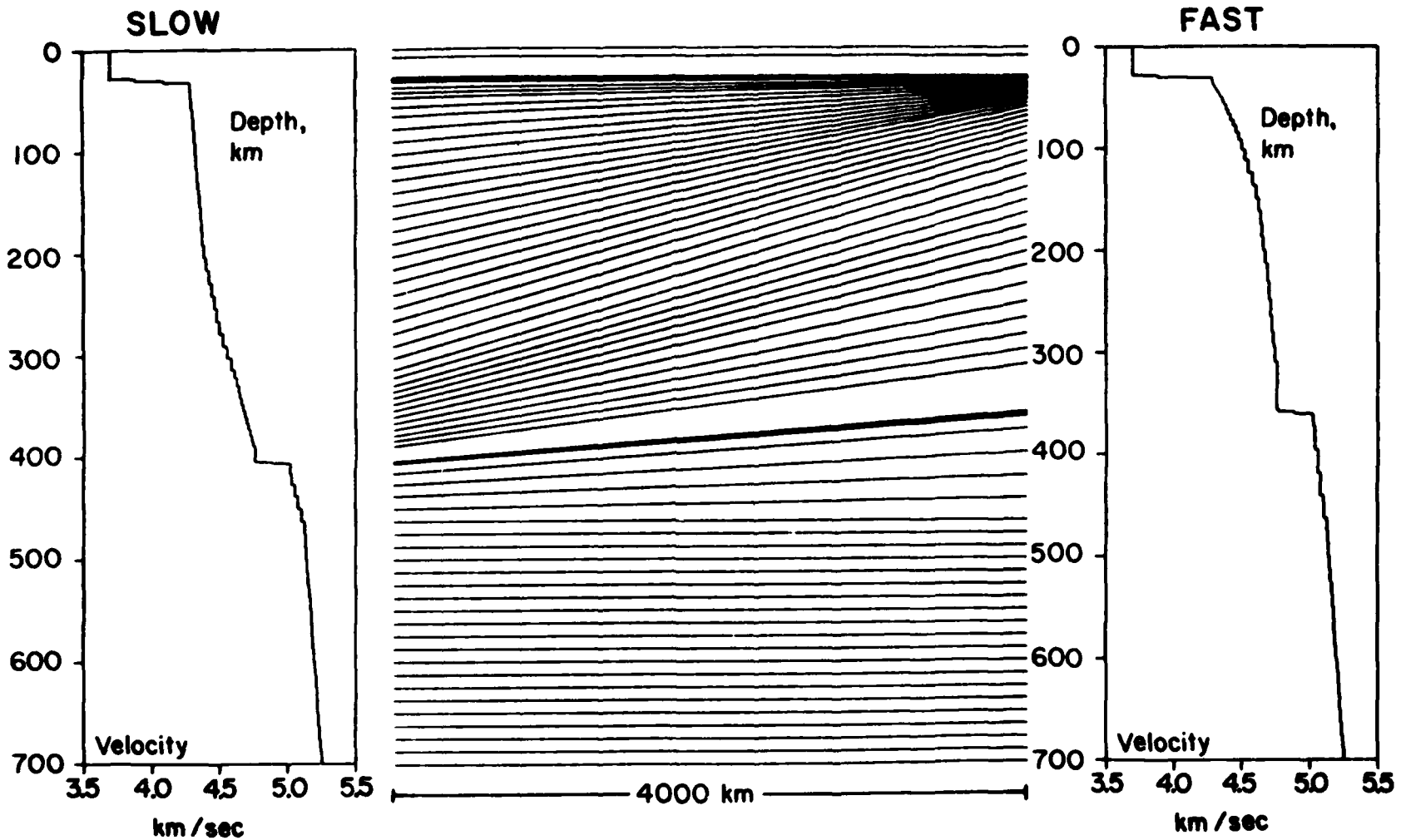

Figure 11: Cross-section displaying isovelocity lines and accompanying starting and ending model.

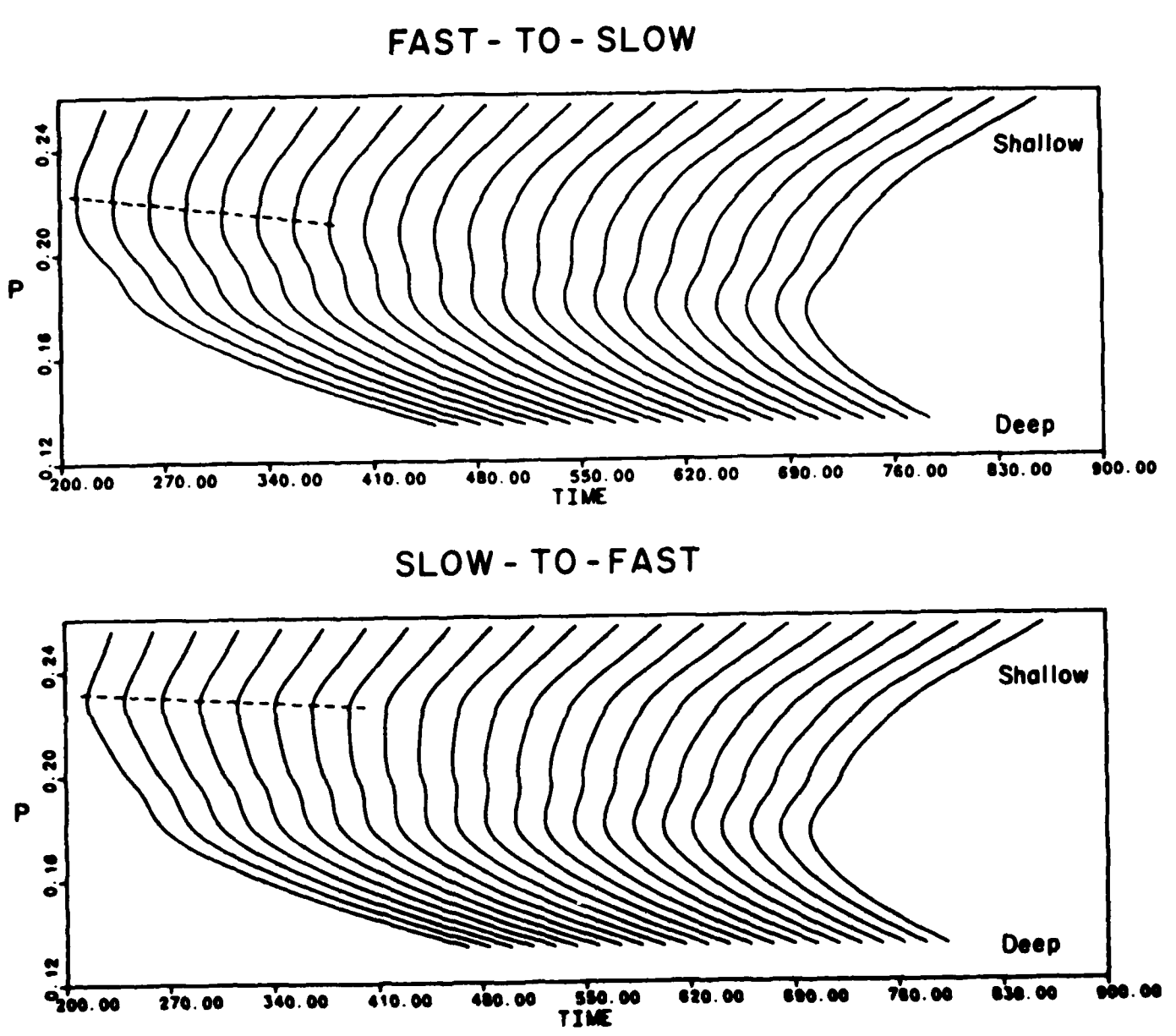

Figure 12: Sets of (p) vs (t) curves for possible receivers along a profile from 8 to 30°.

profiles. The largest ray parameter, p_{max}, is .26 which corresponds to the crustal velocity of 3.9. Next, we perform the numerical derivative ($\delta p / \delta t$) of these curves. Note that there will be a large truncation phase at the near stations at p_{max}. This can be avoided by including the product of the transmission coefficients, TC's, across the Moho, the reference interface discussed earlier, since TC(p_{max}) is small. Thus, the product of the TC's with ($\delta p / \delta t$) has a relatively smooth behavior. The head wave along the Moho is added in by including the reflected generalized ray. By performing the convolution indicated in expression (29) we derive step responses from (t vs. p) curves displayed in Fig. 12. These results are shown in Fig. 13. Short period synthetics are included to emphasize the rapid decay of amplitude at the triplication tips. Eliminating the truncation phase discussed here can also be achieved by a modification of the Gaussian beam technique as developed by Madariaga and Papadimitriou (1984).

The synthetics at the smallest ranges are completely controlled by the shallow structure and the local model. Thus, the first arrival from the Fast-to-Slow synthetics has a shorter travel time which causes the triplication from the 400 km discontinuity to arrive later than in the reverse profile.

A more detailed plot of the Slow-to-Fast profile is displayed in Fig. 14 along with the GRT responses for comparison. The synthetics are appropriate for the WWSSN long period system. A typical strike-slip source was assumed with a triangular time history of (1, 1, 1 secs) and a $t^* = 3$, see Grand and Helmberger (1984a).

Note that there is a distinct change in the latter portion of the WKBJ step responses between 17° and 18°. This is caused by omitting the head waves from along the top of the model for distances beyond 17°. However, no apparent change in the synthetics occurs at this range suggesting that the long period drift is outside the pass-band of the operators used in generating these synthetics. The high-frequency spikes so apparent in the GRT step responses are like-wise removed by the convolution operators.

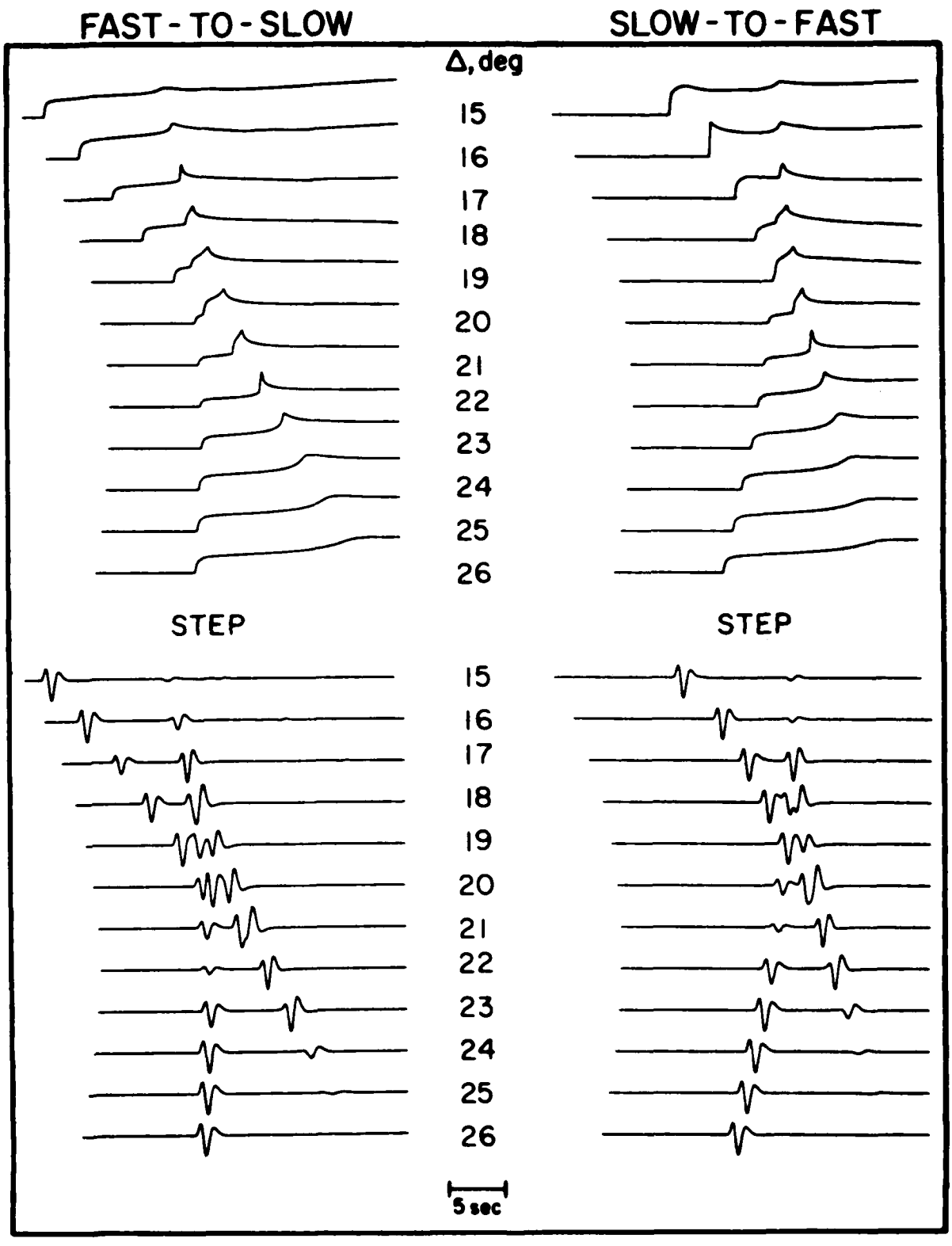

Figure 13: Seismic sections plotted on the same reduced time scale. $t - \Delta/xx$. The synthetics are appropriate for a short period WWSSN instrument response.

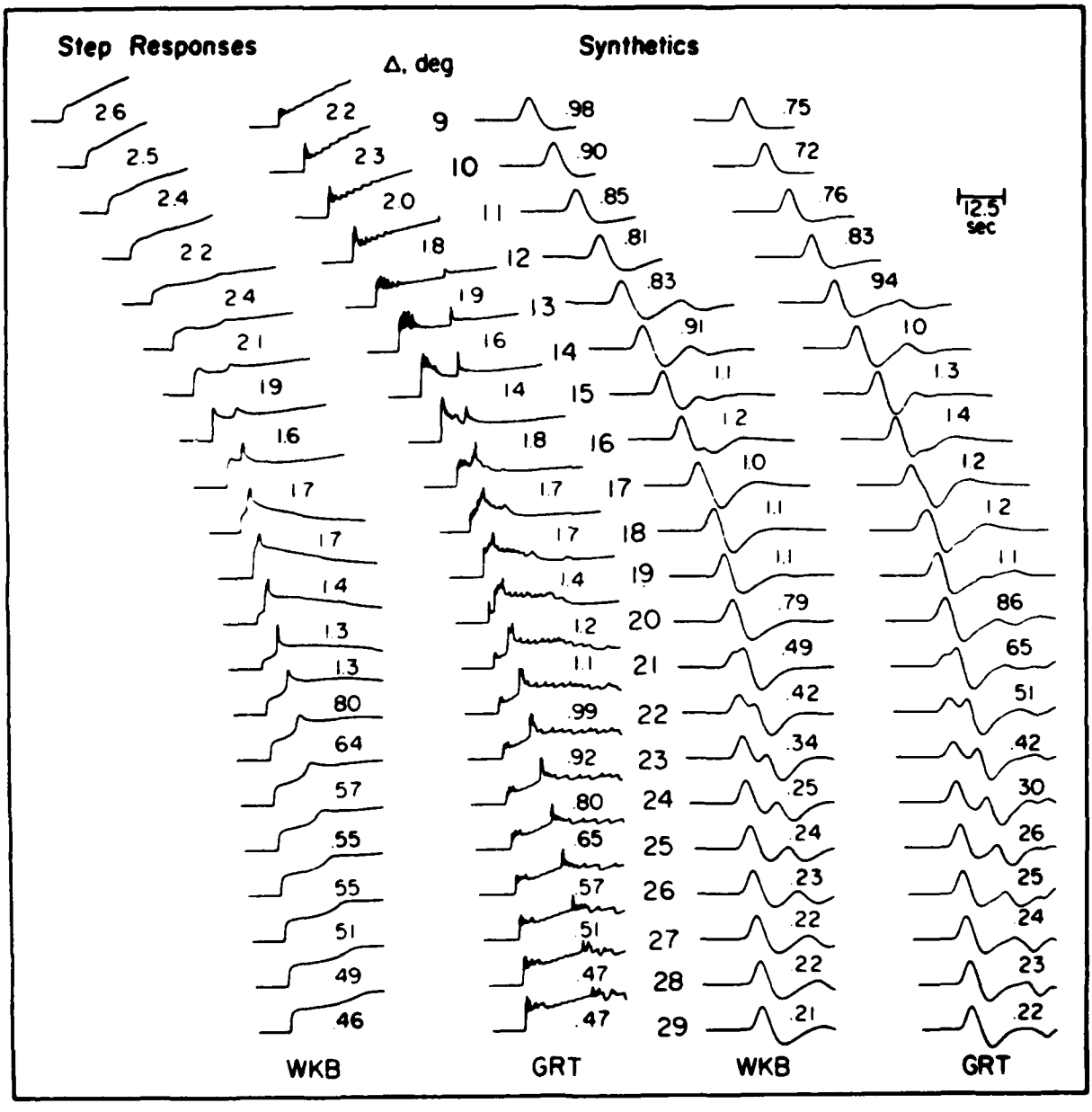

Figure 14: Step responses and synthetics generated by the WKBJ and GRT methods for the Slow-to-Fast model displayed in Fig. 11. The numbers associated with each trace indicate the maximum amplitude.

The 400 km discontinuity is treated slightly differently in the two methods which leads to some shifts in the triplication position. In GRT, the 400 km discontinuity is generally treated as a sharp jump in velocity since this leads to the best results when compared against reflectivity, see Burdick and Orcutt (1978). On the other hand, WKBJ requires a smooth transition, 3 km transition in this particular case, such that the (p vs. t) curve is smooth. Thus, the sharp spikes occurring in the GRT step responses near 14^{o} are precritical angle reflections from the 400 km discontinuity. Similarly, the triplication seems to extend to greater distances in the GRT results. Note that the most severe mismatch occurs near this range. At larger ranges the two methods agree quite well, especially the synthetic waveforms. In fact, the synthetic waveforms agree at all distances with the maximum deviation in amplitude of about 25%. And, since these synthetic waveforms are used to interpret observations which can seldom be modeled as well as the agreement between these two methods, we can consider the WKBJ modifications successful. For more precision involving sharp boundaries we suggest breaking the p integration into a combination of WKBJ for the smooth portion of the model and a generalized ray for the reflecting interface, for example see Given (1984).

Conclusions

In this paper we presented a hybrid procedure of generating complete seismograms in laterally varying structure by applying a mixture of GRT and WKBJ methods. First, we reviewed the modifications of GRT required for dipping structure in terms of local coordinates and ray parameter concepts for line and point source theory. Solutions calculated by this approach not only agree with geometric results, but also agree with longer period motions such as computed with finite-difference methods. Using the correspondence between GRT and WKBJ theory, we can express the latter in relatively simple form, essentially applying a square-root of distance correction to line source spreading. Comparisons between GRT and WKBJ synthetics of diving energy paths

agree reasonably well. Thus, we can construct nearly complete seismograms with a combination of GRT and WKBJ with the former used to handle the shallow structure. Some useful demonstrations of the methods are given for crustal and upper-mantle models.

References

Apsel, R. J. and J. E. Luco (1983). On the Green's functions for a layered halfspace, Part II., Seismol. Soc. Amer., Bull, 73, 931-952.

Burdick, L. J. and J. A. Orcutt (1978). A comparison of the generalized ray and reflectivity methods of waveform synthesis, Geophys. J., 58, 261.

Cerveny, V., M. M. Popov and I. Psencik (1982). Computation of seismic wave fields in inhomogeneous media, Gaussian beam approach, Geophys. J., 70, 109-128.

Chapman, C. H. (1976). A first-motion alternative to geometrical ray theory, Geophys. Res. Letts., 3, 153-156.

Chapman, C. H. (1978). A new method for computing synthetic seismograms, Geophys. J., 54, 481-518.

Chapman, C. H. and R. Drummond (1982). Body-wave seismograms in inhomogeneous media using Maslov Asymptotic Theory, Seismol. Soc. Amer., Bull., 72, 277-318.

Forsyth, D. W. (1975). The early structural evolution and anisotropy of the oceanic upper-mantle, Geophys. J., R. astr. Soc., 43, 103-162.

Frazer, L. N. and R. A. Phinney (1980). The theory of finite frequency synthetic seismograms in inhomogeneous elastic media, Geophys. J., R. astr. Soc., 63, 691-717.

Gilbert, F. and L. Knopoff (1961). The directivity problem for a buried line source, Geophysics, 26, 626-634.

Given, J. (1984). Inversion of body-wave seismograms for upper mantle structure. Ph.D. Thesis, California Institute of Technology, Pasadena, California 91125.

Grand, S. P. and D. V. helmberger (1984a). Upper mantle shear structure beneath the northwest Altantic Ocean, J. Geophy. Res., in press.

Grand, S. P. and D. V. Helmberger (1984b). Upper mantle shear structure of North

America, Geophys. J., R. astr. Soc., 76, 399-438.

Helmberger, D. V. (1973). Numerical seismograms of long-period body waves from seventeen to forty degrees, Seismol. Soc. Amer., Bull., 63, 633-646.

Helmberger, D. V. (1983). Theory and Application of Synthetic Seismograms. Proceedings of the International School of Physics, Cource LXXXV, edited by H. Kanamori and E. Baschi, North Holland press.

Helmberger, D. and S. Malone (1975). Modeling local earthquakes as shear dislocations in a layered half space, J. Geoph. Res., 80, 4881-4888.

Hong, T. L. and D. V. Helmberger (1977). Generalized ray theory for dipping structure, Seismol. Soc. Amer., Bull., 67, 995-1008.

Hong, T. L. and D. V. Helmberger (1978). Glorified optics and wave propagation in nonplanar structure, Seismol. Soc. Amer., Bull., 68, 1313-1330.

Hudson, J. A. (1963). SH waves in a wedged-shaped medium, Geophys. J., R. astr. Soc., 7, 517-546.

Madariaga, R. and P. Papadimitriou (1984). Gaussian Beam Modeling of Upper Mantle Phases, submitted to Annales Geophysicae.

Vidale, J., D. V. Helmberger and R. W. Clayton (1984). Finite-Difference Seismogram for SH-waves, to be submitted to Seismol. Soc. Amer., Bull.

Wesson, R. L. (1970). A time integration method for computation of the intensities of seismic rays, Seismol. Soc. Amer., Bull., 60, 307-316.

Wiggins, R. A. (1976). Body wave amplitude calculations, II, Geophys. J, R. astr. Soc., 46, 1-10.

III. A Stable Free-Surface Boundary Condition for 2D Elastic Finite-Difference Wave Simulation

One of the persistent problems in finite-difference solutions of the elastic wave equation is the limited stability range of the free-surface boundary condition, and its behavior with lateral variations in velocity and density. The centered difference approximation (CDA) presented by Alterman and Karal (1968), for example, remains stable only for $\beta/\alpha > 0.30$, where β and α are the shear and compressional wave velocities. The one-sided approximation (OSA) (Alterman and Rotenberg, 1969) and composed approximation (Ilan et al., 1975) have similar restrictions. The revised composed approximation (CA) of Ilan and Loewenthal (1976) has overcome this restriction, but apparently cannot properly handle laterally varying media.

In the first part of this paper we present a free-surface boundary approximation that is itself stable for all physical β/α ratios and is correct for laterally varying media. When the proposed boundary conditions are coupled with second- and fourth-order approximations for the elastic wave equation, the overall problem is stable for β/α greater than 0.01 and β/α greater than 0.02, respectively. A simple numerical test of the method and a comparison with other published methods is given in the second section.

FREE-SURFACE BOUNDARY CONDITIONS

The two-dimensional free-surface boundary conditions of zero tangential and normal stress are

$$\frac{\partial u}{\partial z} + \frac{\partial w}{\partial x} = 0 \tag{1}$$

$$\gamma \frac{\partial u}{\partial x} + \frac{\partial w}{\partial z} = 0 \tag{2}$$

where u and w are the horizontal and vertical displacements, x and z are the horizontal and vertical spatial coordinates, and γ is $(1 - 2\alpha^2/\beta^2)$. To apply finite-differences to equations (1) and (2), an extra row is introduced above the actual free surface. The

geometry is shown in Figure 1. The standard finite difference approximations to the elastic wave equation (Kelly et al., 1976) can be used to determine the solution on the interior of the mesh, up to and including row 1. Previous free-surface boundary conditions cited above have used explicit finite-difference approximations to determine the row 0. This approach can lead to stability restrictions in terms of the β/α ratio and problems with laterally varying media due to the difficulty in centering the normal and tangential derivatives at the same time as averaging laterally varying media parameters.

The method proposed here uses an implicit formulation which centers both the normal and tangential derivatives at the free surface which is halfway between row 0 and row 1. The scheme is similar in concept to the Crank-Nicholson method for the diffusion equation (e.g., Claerbout, 1976, p. 185). Applying centered second-order differences to equations (1) and (2), we have

$$\mathbf{u}_0 - \frac{1}{4} B\ \mathbf{w}_0 = \mathbf{u}_1 + \frac{1}{4} B\ \mathbf{w}_1 \tag{3}$$

$$\mathbf{w}_0 - \frac{1}{4} \Gamma B\ \mathbf{u}_0 = \mathbf{w}_1 + \frac{1}{4} \Gamma B\ \mathbf{u}_1 \tag{4}$$

where the subscripts denote the solution on rows 0 and 1, Γ is a diagonal matrix which contains the values of γ across the surface, and B is a bi-diagonal matrix with sub- and super-diagonals equal to -1 and 1 respectively. Note that the centering of the x derivatives is achieved by averaging estimates on rows 0 and 1.

Equations (3) and (4) can be reduced to separate systems for the vector unknowns $\mathbf{u}_0$ and $\mathbf{w}_0$

$$(\mathbf{I} - \frac{1}{16} \mathbf{B}\,\Gamma\,\mathbf{B})\,\mathbf{u}_0 = (\mathbf{I} + \frac{1}{16} \mathbf{B}\,\Gamma\,\mathbf{B})\,\mathbf{u}_1 + \frac{1}{2} \mathbf{B}\,\mathbf{w}_1 \tag{5}$$

$$(\mathbf{I} - \frac{1}{16} \Gamma\,\mathbf{B}^2)\,\mathbf{w}_0 = (\mathbf{I} + \frac{1}{16} \Gamma\,\mathbf{B}^2)\,\mathbf{w}_1 + \frac{1}{2} \Gamma\,\mathbf{B}\,\mathbf{u}_1 \tag{6}$$

The matrices on the left side of equations (5) and (6) are pentadiagonal and can be solved rapidly by an algorithm that is a simple extension of the standard tridiagonal solver (e.g. Claerbout, 1976, p. 189). The vectors on the right side can be computed

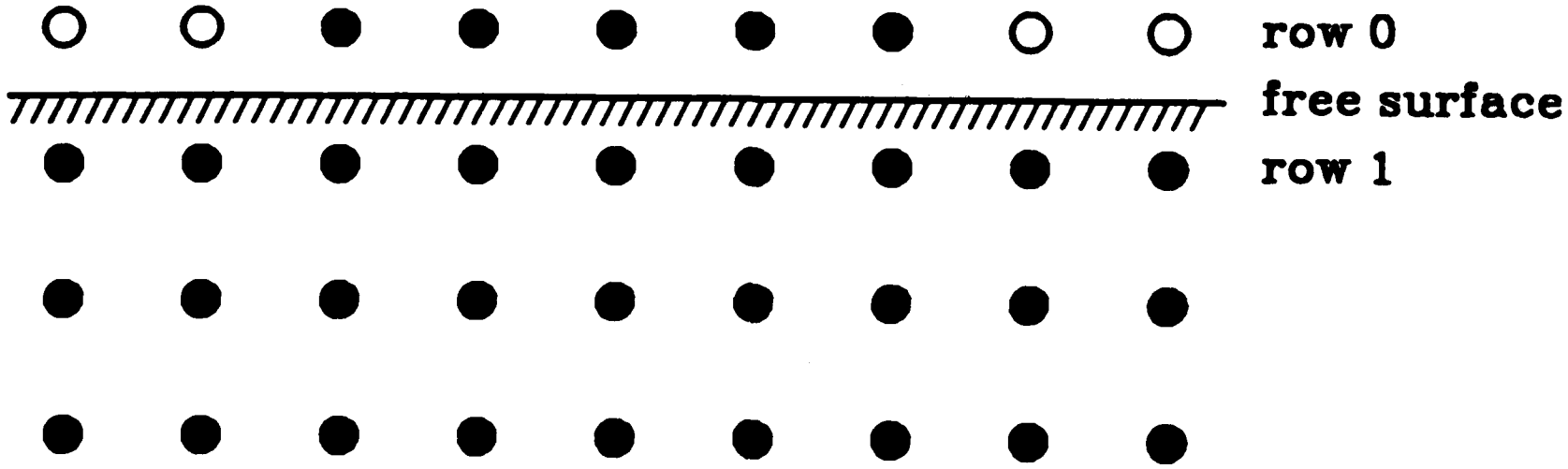

Figure 1. Free-surface geometry. Row 0 is a fictitious row added to allow finite-differences of tangential derivatives. The true free surface lies half-way between row 0 and row 1. The open circles require special treatment in the boundary conditions.

from displacements on row 1.

To show the stability of equations (5) and (6) as extrapolation operators, we Fourier transform over x. This leads to the system

$$\begin{bmatrix} u_0 \\ w_0 \end{bmatrix} = \frac{1}{1 + \gamma \sin^2 kh} \begin{bmatrix} 1 & i \sin kh \\ i\gamma \sin kh & 1 \end{bmatrix} \begin{bmatrix} u_1 \\ w_1 \end{bmatrix} \tag{7}$$

where u and w now denote the Fourier duals of u and w, k is the dual of x, and h is the horizontal mesh spacing. The eigenvalues of the matrix in equation (7) are unity which means that the boundary conditions are stable. To show that the combined problem of the boundary conditions and the interior solution is stable is beyond the scope of this note. In numerical tests, the combined problem remains stable for β/α greater than 0.01 for a second-order interior method, and β/α greater than 0.02 for a fourth-order method. We suspect that the stability problem lies with the interior solutions rather than the boundary conditions for β/α of 0.

EDGES OF THE FREE-SURFACE

The boundary conditions derived above must be modified for the extreme two edge elements on each side of the free surface, which are shown as open circles in Figure 1. For these points, we apply the B1 absorbing boundary conditions of Clayton and Engquist (1977). For the component u on the left side the boundary conditions in equation (5) are modified to be

$$(1 + \delta){u_0}^t + (1 - \delta){u_1}^t = (1 - \delta){u_0}^{t-1} + (1 + \delta){u_1}^{t-1} \tag{8}$$

$$(1 + \delta){u_1}^t + (1 - \delta){u_2}^t = (1 - \delta){u_1}^{t-1} + (1 + \delta){u_2}^{t-1} \tag{9}$$

where $\delta = \alpha \Delta t / h$, and h is the mesh spacing and Δt is the time step. Here (u_0, u_1, u_2) are the first three elements of the vector $\mathbf{u}_0$, and the superscripts t and $t-1$ refer to the present and previous time step. Stability of equations (8) and (9) is independent of the β/α ratio. These equations most effectively absorb horizontally traveling P-waves. Similar equations are used for the vertical component w, except that

$\delta = (\beta \Delta t) / h$ is used to absorb horizontally traveling S-waves. Mirror images of these conditions are used at the right edge of the free surface.

NUMERICAL EXAMPLES OF STABILITY AND ACCURACY

The accuracy of the proposed implicit approximation (IA) is shown in Figure 2. The CA and CDA, which are not shown, are about as accurate as the IA because all three are accurate to second-order. The OSA, which is also not shown, is only accurate to first order and therefore introduces more error at the shorter wavelengths. Both the direct and the Rayleigh wave agree with the analytic calculation. The slight difference in sharpness between the analytic and the finite difference traces is due to grid dispersion in the finite difference method. The small perturbations to the Rayleigh wave are shear wave noise which comes from the source region.

The stability of the proposed free surface boundary conditions is illustrated by calculations for the vertical component of a half-space problem where β/α is 0.2. These results are shown in Figure 3. The CA and IA are well-behaved, while the OSA and CDA are not. The slight difference in amplitude between the CA and IA results from the slight difference in the free surface position, which is half a mesh spacing further from the source with the CA method than with the IA method. The results for the stability of the OSA, CDA, and CA are in agreement with those found by Ilan and Loewenthal (1976).

A test with lateral heterogeneity is shown in Figure 4. The velocities within the rectangle under the receiver are a factor of three less than the velocities in the halfspace. The OSA is inaccurate, particularly on the horizontal component. The CDA is unstable. The CA is more gently unstable, but in our experience, structure with more lateral variation causes the method to become unstable more rapidly. Part of the disagreement between the CA and the IA in the early part of the record arises from the slightly different location of the free surface mentioned above. Only the IA results in energy dying away with time in the signal. We suspect the result is accurate, but we have no method with which it may be conveniently checked.

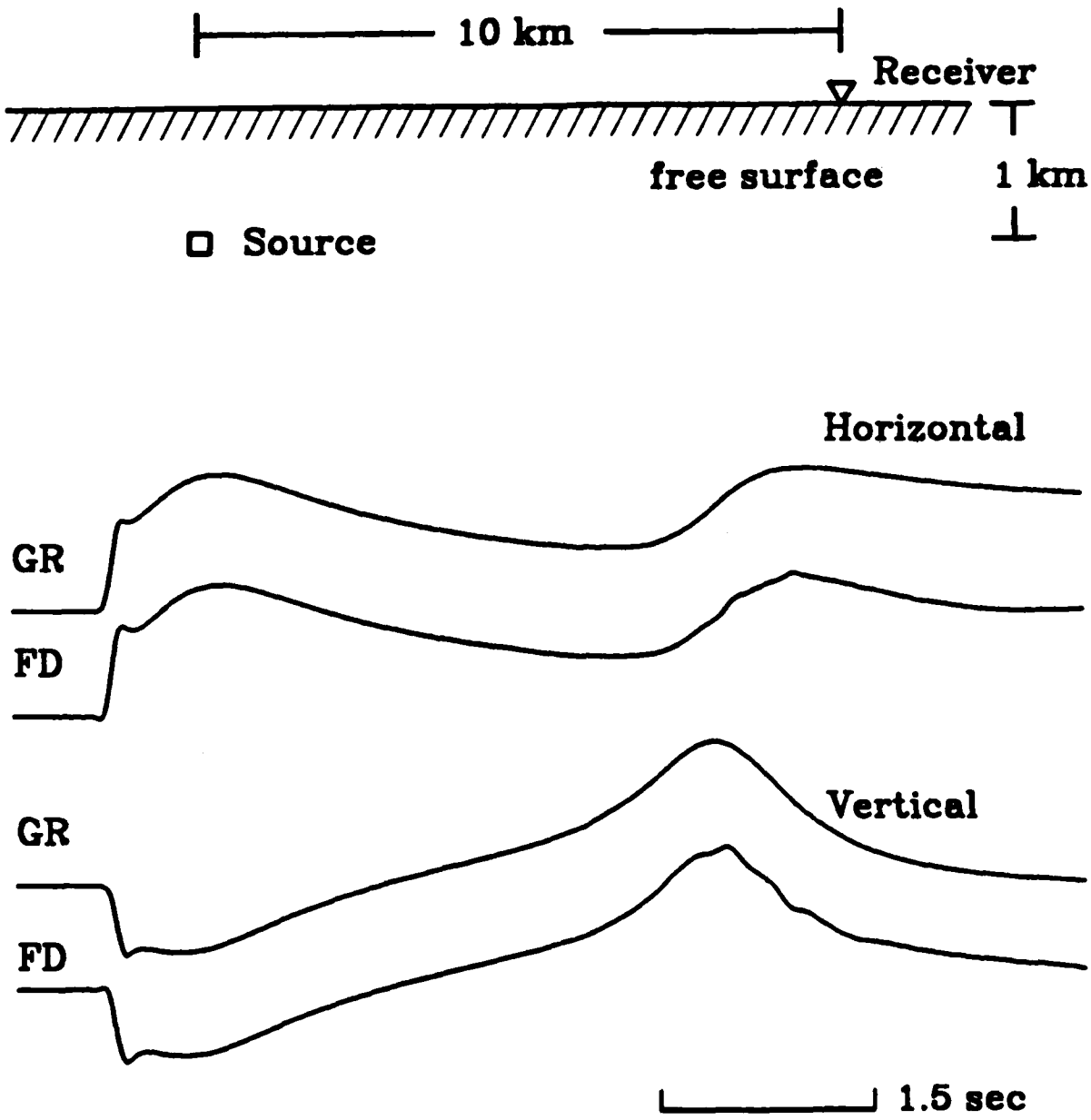

Figure 2. The analytic result for a halfspace with an explosive line source is compared to a fourth-order finite difference solution with the implicit free-surface boundary condition. The analytic result is calculated by the method of de Hoop (1960). In the halfspace, α is 3.5 km/sec and β is 1.5 km/sec.

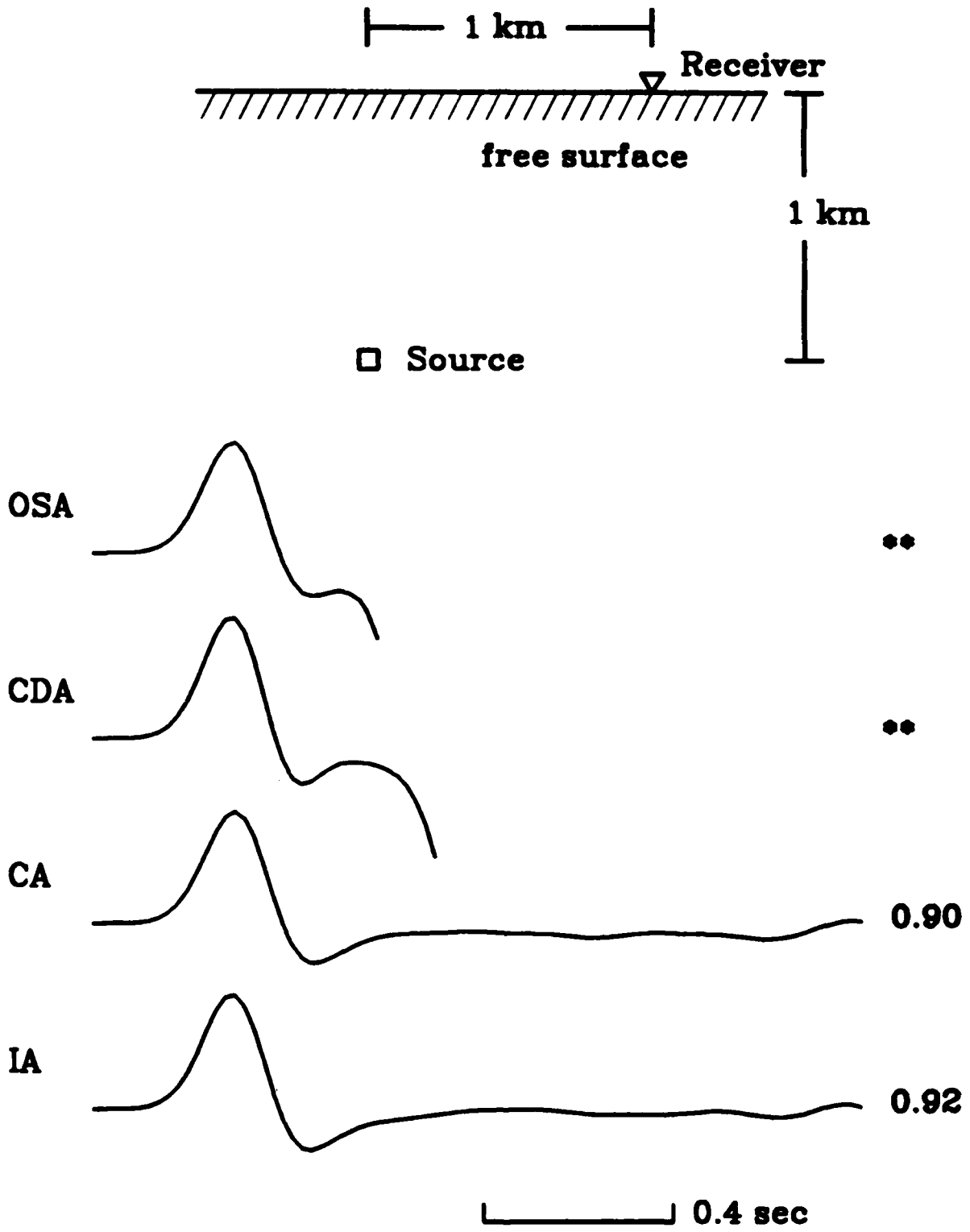

Figure 3. The vertical component for the one-sided (OSA), central-difference (CDA), composed (CA), and implicit (IA) approximations of the free-surface boundary conditions are shown for the small β/α ratio of 0.2. Traces are dotted where they go off-scale. Peak amplitudes are given to the right of each trace. In the halfspace, α is 3.5 km/sec and β is 0.7 km/sec. An explosive line source is used.

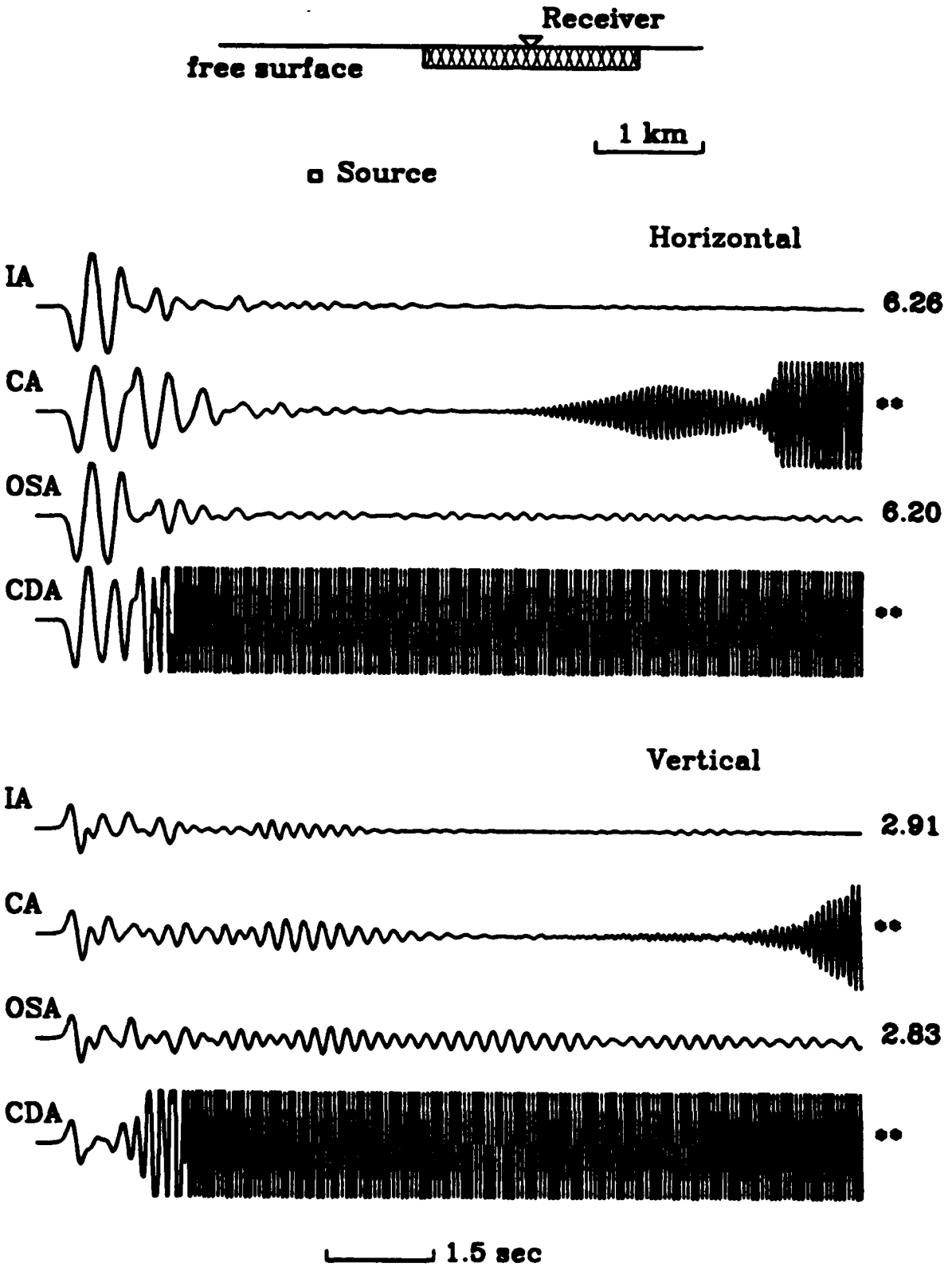

Figure 4. The horizontal and vertical component for the one-sided (OSA), central-difference (CDA), composed (CA), and implicit (IA) approximations of the free-surface boundary conditions are shown for laterally varying structure. In the hatched region, which is 2.0 km wide and 0.1 km deep, α is 1.3 km/sec, β is 0.6 km/sec, and ρ is 1.0 g/cc. In the rest of the halfspace, α is 3.5, β is 2.0, and ρ is 2.6. Peak amplitudes are given to the right of each trace. An explosive line source is used.

The only free surface which is stable for both low β/α ratios and for lateral heterogeneity is the implicit scheme proposed in this note.

REFERENCES

Alterman, Z., and F.C. Karal, 1968. Propagation of elastic waves is layered media by finite difference methods; *Bull. Seism. Soc. Am.* , 58: pp. 367-398.

Alterman, Z., and A. Rotenberg, 1969. Seismic waves in a quarter plane; *Bull. Seis. Soc. Am.* , 59: pp. 347-368.

Claerbout, J.F., 1976. *Fundamentals of Geophysical Data Processing*, McGraw-Hill, New York.

Clayton, R.W., and B. Engquist, 1977. Absorbing boundary conditions for acoustic and elastic wave equations; *Bull. Seis. Soc. Am.* , 67: pp. 1529-1540.

de Hoop, A.T., 1960. A modification of Cagnaird's method for solving seismic pulse problems; *Appl. Sci. Res.* , B8: pp. 1-42.

Ilan, A., A.U. Ungar, and Z. Alterman, 1975. An improved representation of boundary conditions in finite difference schemes for seismological problems; *Gephys. J. R. astr. Soc.* , 43: pp. 727-745.

Ilan, A., D. Loewenthal, 1976. Instability of finite difference schemes due to boundary conditions in elastic media; *Geophys. Prosp.* , 24: pp. 431-453.

Kelly, K.R., R.W. Ward, S. Treitel, and R.M. Alford, 1976. Synthetic seismograms: a finite-difference approach, *Geophysics* , 41, pp. 2-27.

END

FILMED

5-86

DTIC